Thesis for the Degree of Licentiate of Engineering

Studies of catalyst sintering during operating conditions

Pooya Tabib Zadeh Adibi

Department of Applied Physics

Chalmers University of Technology

Göteborg, Sweden 2014

Studies of catalyst sintering during operating conditions
Pooya Tabib Zadeh Adibi

Department of Applied Physics
Chalmers University of Technology
SE-412 96 Göteborg
Sweden
Telephone + 46 (0)31-772 3373

Cover picture:
Change in indirect nanoplasmonic signal during sintering of Pt nanoparticles. The TEM images show the Pt particles on one gold sensor particle before and after the sintering.

Printed at Chalmers Reproservice
Göteborg, Sweden 2014

Studies of catalyst sintering during operating conditions
Pooya Tabib Zadeh Adibi
Department of Applied Physics
Chalmers University of Technology

Abstract

The damaging effect of pollutants from exhaust gas of combustion engines on the human health and the environment is well recognized. Since the 70s, the three-way catalytic converter (TWC) has substantially improved the urban air quality by simultaneous conversion of CO, NO_x and unburned hydrocarbons to O_2, N_2, CO_2 and H_2O. The active phase in the TWC is small precious metal particles (e.g. platinum, palladium, and rhodium) that are dispersed on a high surface area oxide support such as γ-alumina. One issue regarding the TWC is their limited durability due to the catalyst deactivation during operation. Sintering of nanometer sized metal particles at high temperature is one of the major reasons for the deactivation. Detailed understanding of sintering mechanisms and kinetics are crucial to design catalyst formulations with extended durability. However, the lack of suitable methods to follow particle sintering under technologically relevant conditions hinders the progress in this area.

The present thesis addresses fundamental issues connected to platinum sintering on oxide supports by use of indirect nanoplasmonic sensing (INPS) and transmission electron microscopy (TEM). Moreover, indirect nanoplasmonic sensing is further developed as an operando tool for characterization of sintering processes on different supports and in different gas environments. In particular, the sintering kinetics and evolution of particle size distributions are studied during oxidizing conditions on alumina and silica. In the first part of this study, high time resolution sintering kinetic data are deduced by correlating the INPS data with ex situ TEM analysis. The obtained kinetic data are based on ensemble average of particles. Thus, to further study Pt sintering in more details, intermittent particle size distributions are analyzed as a function of time and temperature. Transitional bimodal size distributions are clearly observed during sintering of Pt on the two investigated supports.

Keywords: platinum, catalyst deactivation, nanoparticle sintering, sintering kinetics, operando spectroscopy, indirect nanoplasmonic sensing

List of appended papers

This thesis is based on the following publications:

Paper I

In situ plasmonic sensing of platinum model catalyst sintering on different oxide supports in O_2 and NO_2 atmosphere
Pooya Tabib Zadeh Adibi, Francesco Mazzotta, Tomasz J. Antosiewicz, Magnus Skoglundh, Henrik Grönbeck, and Christoph Langhammer
Submitted to ACS Catalysis

Paper II

Transitional bimodal particle size distributions during Pt sintering on alumina and silica
Pooya Tabib Zadeh Adibi, Vladimir P. Zhdanov, Christoph Langhammer, and Henrik Grönbeck
In manuscript

My contributions to the papers

Paper I

Except the INPS measurement of sintering in NO_2, I performed all the experiments and the corresponding analysis. I wrote the first draft of the manuscript.

Paper II

I performed all the experiments and the corresponding analysis. I wrote the first draft of the manuscript.

Contents

1 Introduction

Exhaust from combustion engines contains gases that are toxic for both humans [1] and the environment. The major pollutants are carbon monoxide (CO), nitrogen oxides (NO_x), unburned hydrocarbons, and particulate matter (e.g. soot). To control the emissions, legislative regulations have been established, starting with the Clean Air Act in the United States in 1970. Since then, similar regulations have been implemented worldwide. One of the first successful strategies to meet the regulations was the introduction of the three-way catalytic converter (TWC), which enables simultaneous reduction of NO_x to N_2, and oxidation of CO and hydrocarbons to H_2O, and CO_2. The key components of the TWC are precious metal particles such as platinum (Pt), Palladium (Pd), and Rhodium (Rh). Together with ceria and stabilizers, the particles are generally dispersed on a high surface area oxide such as γ-alumina.

A catalytic converter should meet the standards with respect to the emissions and maintain that over time. For example, the EU5/EU6 legislations require the TWC to meet the standards after 100,000 km or five years of usage [2]. One of the issues regarding catalytic converters is that they deactivate during operation [3]. Thermal damage, poisoning, and mechanical damage are the major causes of deactivation. One type of thermal damage is sintering of metal particles at high temperature, which leads to the formation of larger particles due to the substantial surface to volume ratio of small particles. Therefore, the active metal

surface area on which reactions occur is reduced over time, which leads to lower efficiency. Due to deactivation, TWC manufacturers must design a fresh catalyst that performs well below the emission regulations. Excessive use of platinum group metals (Pt, Pd, and Rh) has considerable impact on the environment and industry. For example, mining of platinum group metals is associated with point-source pollution and mining waste at the extraction and refining sites [4]. Note that the automotive after-treatment is the largest market for platinum group metals. In 2012, automotive catalytic converters accounted for 56 % of the gross world demand for Pt, Pd, and Rh [5].

Successful designs have increased the stability of supported particles [6] but there is still a considerable room for improvement. Despite the large amount of studies, a detailed understanding of sintering in different conditions and catalyst systems is missing. One reason alongside the complexity of the sintering processes is the lack of suitable methods to follow the sintering processes under realistic conditions. Techniques such as X-ray spectroscopy provide information relevant to real catalysis, but have the drawback that they need synchrotron light, which generally is expensive with limited access time. Another alternative is ex situ studies of catalyst in the TWC after aging, which does not provide direct insight on the mechanism.

In Paper 1, Indirect nanoplasmonic sensing (INPS) is employed together with transmission electron microscopy (TEM) to monitor Pt sintering on flat supports, under realistic conditions. In situ INPS allows monitoring of sintering by visible light that makes the experimental setup relatively simple. The flexibility of INPS to follow sintering of Pt particles on different supports (alumina and silica), and in different gaseous environment (O_2 and NO_2) is demonstrated. Paper 2 examines the time-resolved and temperature-resolved evolution of particle size distribution of sintered supported Pt, and the formation of a transitional bimodal size distribution.

The thesis is structured as follows. Chapter 2 introduces the concept of heterogeneous catalysis and describes different deactivation mechanisms. Sintering of supported particles, that is the central topic of the studies, is explained in detail. Chapter 3 presents the experimental techniques used in this work, with focus on indirect nanoplasmonic sensing. Chapter 4 is dedicated to the sample fabrication. Chapter 5

summarizes the results, and finally, conclusions and outlook is provided in chapter 6.

2 Catalyst deactivation

Catalysis is a phenomenon in which a chemical reaction is accelerated by a substance called catalyst. Every one of us constantly experience catalysis; from enzymes (biocatalyst) in our bodies that accelerate vital biological reactions like building up DNA, to breathing cleaner air provided by catalytic converter in vehicles. The active catalytic phase may exist in several different forms including atoms, molecules, or particles. Catalysis could be divided into homogeneous, heterogeneous and enzymatic. In homogeneous catalysis, the catalyst and the reactants are in the same phase (gas or liquid), while in heterogeneous catalysis, the phase of the reactants and the catalyst differs from each other. Enzymatic catalysis refers to processes in which enzymes catalyze biological reactions [7].

2.1 Heterogeneous catalysis

In many practical heterogeneous catalysis, reactions occur on the surface of a solid catalyst. Thus, in order to achieve high percentage of exposed atoms and use the catalyst economically, nanometer-sized metal particles are often dispersed on mesoporous supports such as alumina or silica. In addition, smaller particles may exhibit an enhanced catalytic activity. Gold is one example, which shows activity for oxidation reactions below a certain size regime [8, 9].

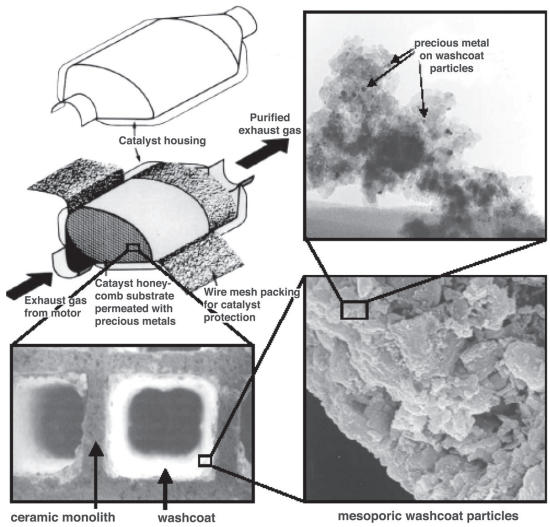

Figure 2.1: Illustration of three-way automotive catalytic converter (TWC). (Top left) Schematic of the TWC housing and the ceramic honeycomb. (Bottom left) SEM image of honeycomb channels coated with washcoat layer, (bottom right) SEM image of mesoporous washcoat, (top right) TEM image of catalyst nanoparticles supported on washcoat material. Reprinted from [10].

One important application of heterogeneous catalysis is the automotive three-way catalytic converter (TWC). Figure 2.1 illustrates the typical structure of a TWC. It consists of a ceramic monolith that is coated with 20-50 μm layer of high surface area washcoat such as γ-alumina. The precious metal components of TWC are Pt, Pd, and Rh, which are dispersed on the washcoat material.

TWC enables three main reactions, namely the oxidation of CO and unburned hydrocarbons (HC), as well as the reduction of NO_x. Oxidation reactions are catalyzed most efficiently by Pt and Pd, while Rh is the superior catalyst for NO_x reduction.

To elucidate the concept of heterogeneous catalytic reactions, catalytic CO oxidation is taken as an example (Figure 2.2). The catalytic cycle begins with adsorption of CO and O_2 on the surface of the catalyst where the O_2 molecule dissociates into two oxygen atoms. The adsorbed O atom and CO molecule react on the catalyst surface to form stable CO_2 that is weakly bonded to the surface, and thus, desorbs and frees

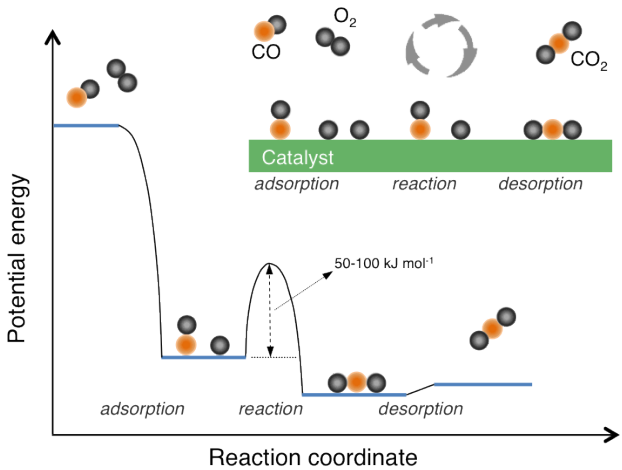

Figure 2.2: Potential energy diagram of CO oxidation by a catalyst. The inset shows the schematics of catalytic cycle including adsorption of reactants on catalyst surface, surface reaction and final desorption of product. Adapted from [7].

sites for the next catalytic cycle [7]. Figure 2.2 shows the schematic potential diagram and reaction cycle for catalytic oxidation of CO. The key point is that the activation energy for breaking the O-O bond in a gas phase reaction without catalyst is about 560 kJ mol^{-1}, whereas in the catalytic reaction, the O_2 molecule dissociates easily on the catalyst surface without sizable activation energy. The described reaction path follows what generally is referred to as a Langmuir-Hinshelwood reaction path; the reactants absorb before reacting. One alternative path is the Eley-Rideal scheme, where one of the reactants reacts directly from the gas phase.

2.2 Catalyst deactivation

Inevitably, most catalysts are deactivated during operation at high temperatures and in harsh gas environments. Deactivation is accompanied by reduced activity and/or lower selectivity to the desired products. The degree and time-scale (in the order of seconds to years) of deactivation depends on the catalyst and the operating conditions. Catalyst deactivation leads to high additional costs due to replacement or regen-

eration of the catalyst. However, deactivation can to some extent be prevented, delayed or in some cases reversed. Detailed understanding of deactivation mechanisms could lead to rational design of durable catalyst systems. In the following, six major deactivation mechanisms are discussed, and examples relevant to the TWC are mentioned [3]. Most attention will be paid to sintering of nanoparticles.

(a) Poisoning

Deactivation by poisoning is a mechanism where the number of active catalytic sites is decreased due to the chemisorption of atoms and molecules on the active metal or support surface. Chemisorbed species can influence the active sites in different ways: (1) by physically blocking the metal particles or the washcoat pores and consequently disabling reactant access to metal catalyst, and (2) by inducing changes in electronic and geometric structure of the surface. In some cases, the reactants or products strongly adsorb to the catalyst and act as poison (self-poisoning). The TWC could be deactivated by poisons such as phosphorous (from lubricating oil), lead, and sulfur. In automotive exhaust, sulfur originates from hydrocarbons such as thiophenes, which is oxidized to SO_2 during combustion and blocks the noble metal sites at temperature below 300 °C [7, 11]. Above 300 °C, SO_2 could subsequently be oxidized to SO_3, which also is a poison. Regeneration of SO_x poisoned catalyst is possible by exposing the catalyst to pure oxygen or hydrogen at high temperature. However, such treatments could often introduce problems such as reduction of oxide support (H_2) or oxidation of metal catalyst (O_2).

(b) Solid-state reactions

Solid-state diffusion and reaction at operating conditions might lead to deactivation by transforming the active phase to a non-active phase. An example of such process is decomposition of active PdO species to inactive Pd at temperature higher than 800°C. PdO is generally believed to be more active for catalytic combustion of, e.g. methane, than metallic platinum [3].

(c) Gas/vapor-solid reactions

Gas-solid reactions could deactivate the catalyst by reaction of the va-

por phase with catalyst to produce either an inactive phase or volatile compounds, which exit the catalytic converter. An example of these reactions is the formation of inactive phase of $RuAl_2O_4$ at high temperature, as well as the formation of volatile RuO_4. In general, this form of chemical deactivation can be suppressed by careful design of operating conditions. Formation of volatile compounds could be prevented by operating at a temperature lower than temperature for compound formation, or above the temperature for compound decomposition. Metal stabilizers could also help to resist this process [3].

(d) Fouling

Fouling refers to the deposition of species such as carbon onto the catalyst surface that leads to blockage of active sites and/or pores. On supported metal catalysts, carbon, that could results from unburned hydrocarbons, may (1) partially or totally (encapsulation) absorb on active sites and thereby block access of reactants to catalyst, and/or (2) block pores, which disable access of reactants to the particles inside these pores. In order to prevent fouling, one could consider an operating condition that carbon formation is minimized. If this is not possible, regeneration could be realized by combustion of deposited coke/carbon at low temperature.

(e) Mechanical deactivation

Mechanical failure is often observed due to physical damage. High-pressure drop may cause the catalyst to be crushed. Moreover, erosion of catalyst due to high velocity motion of fluid might yield deactivation. Adding binders can improve the adhesion between washcoat and substrate [12].

(f) Thermal degradation and sintering

Thermal processes result in deactivation of catalysts in several ways; (1) decrease in metal surface area due to growth of catalyst, (2) loss of support surface area and pore collapse, and (3) solid-state reaction that chemically transforms active phase to non-catalytic phase (explained above). The first two phenomena are referred to as sintering, thermal aging, or coarsening. Sintering processes occur at high temperature and depend strongly on temperature. In the TWC, the loss of support

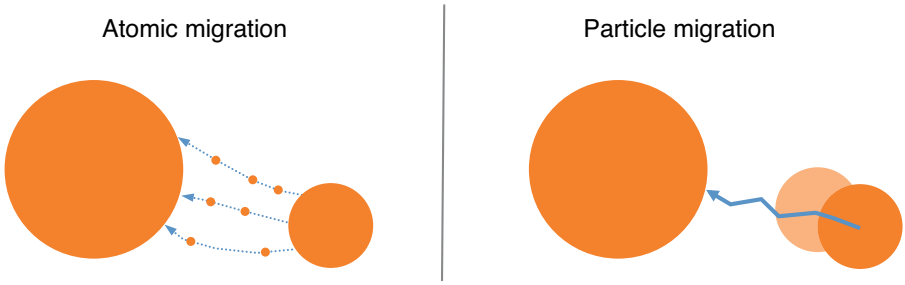

Figure 2.3: Simple illustration of particle sintering mechanisms: (left) atomic migration (Ostwald ripening), and (right) particle migration and coalescence.

is often caused by phase transformation of γ-alumina to phases with lower surface area and pores such as θ-alumina or α-alumina. These irreversible conversions result in the encapsulation of metal particles and the catalyst becomes inaccessible for the reactant. Adding specific amounts of stabilizers, such as BaO, La_2O_3, SiO_2, and ZrO_2, could prevent support sintering. In the following, sintering of supported metal particles is discussed in more detail.

The driving force for nanoparticle sintering is reduction of surface energy by forming larger particles with less under-coordinated atoms. Sintering is a complex physical and chemical process, which is affected by several parameters such as temperature, atmosphere, metal, support and promoter. In automotive catalytic converters, sintering of the precious metals has considerable environmental [4] and economic impact. Detailed understanding of the mechanisms and kinetics of sintering is needed to come up with strategies that could limit the effect of this process. Generally, it is easier to limit or prevent sintering than to reverse it. Lowering the temperature (if possible) is the most direct solution. In recent years, this has been realized in automotive after-treatment by introducing more fuel-efficient vehicles that operate under lean condition and consequently lower temperature (however, at low temperature "cold start" issue arises [13]). In some cases, chemical treatment with O_2 and/or Cl_2 (or other gases) can redisperse the sintered catalyst [14–17].

Two mechanisms for metal particle sintering have been advanced: (1) Atomic migration or Ostwald ripening (named after Wilhelm Ostwald [18]), in which atoms from smaller particles are transported to larger

ones either via surface diffusion on the support or via the vapor phase, and (2) Particle migration, which involves the migration of entire particles over the support, followed by collision and coalescence. Figure 2.3 shows the simple schematics of these mechanisms. Theoretical models describing Ostwald ripening and particle migration are briefly discussed in the following.

During recent decades, several models for sintering and redispersion have been put forward. The models have different bases; thermodynamic models that are based on statistics of ensemble of particles, mechanistic models that deal with processes at the single particle level (e.g. Monte Carlo simulation [19–21]), and empirical models such as the power law expressions.

Ostwald ripening: The difference in chemical potential of particles determines the rate of atomic transport between them. The chemical potential of a particle, , with curvature radius of R can be expressed by the Gibbs-Thomson equation [22].

$$\mu = \mu_0 + 2\gamma\Omega/R \tag{2.1}$$

where μ_0 is the chemical potential of an infinitely large particle, γ is the particle surface energy, and Ω is the atomic volume. Small particles have larger chemical potential, hence, larger particles grow at the expense of smaller ones. Ostwald ripening could in principle have two different rate-limiting steps: (1) detachment of the species from the smaller particles (interface control limited), and (2) diffusion of the detached entities on the surface of the support or through the vapor phase (diffusion control limited). Based on the Gibbs-Thomson relation, Lifshitz and Slyozov [23] and Wagner [24] (LSW) developed a model that statistically describes the Ostwald ripening of spherical particles in a three-dimensional homogenous medium. The LSW model predicts an asymptotic particle size distribution (PSD) that is independent of the initial PSD and does not change with time after a transient period. The characteristic PSD has a tail towards the smaller particle side of the main peak (Figure 2.4 left). Later on, Chakraverty [25] adopted the LSW model for particles (spherical cap) on two-dimensional homogenous support and predicted similar asymptotic PSD shape. According to his model, particles could not grow more than twice the average size

[25].

Wynblatt and Gjostein [22] modeled the growth and decay of individual particles (spherical cap on flat homogenous support), rather than employing a statistical description of an ensemble of particles. Their model establishes the growth rate for both interface controlled and diffusion controlled ripening. The rate equation depends on parameters such as the temperature, the metal-support contact angle, metal surface energy, the diffusivity, and detachment activation energy. Campbell et al. further improved the ripening model by incorporating the size-dependent surface energy of the particles [26, 27].

Particle migration and coalescence: Provided that the particles are given enough energy, atoms on the surface of a particle can move around. When the diffusion length is comparable to the particle diameter, these movements lead to displacement of the particle in a Brownian type motion. The displacement of a particle undergoing Brownian motion is,

$$X = 2\sqrt{D_p t} \tag{2.2}$$

where D_p is particle diffusion coefficient and t is time. Gruber [28] derived this parameter for a spherical bubble migrating in a three-dimensional solid, and later Willertz and Shewmon [29] found an expression for D_p by assuming faceted particles. Another model is binary collision model [30, 31], in which either migration or the coalescence can be the rate limiting step. It has been shown that the PSD for particles that are sintered by particle migration and coalescence can be fitted by a log-normal distribution function that has a tail towards the larger diameter side of the peak (Figure 2.4 right) [32].

According to Figure 2.4, one can imagine that comparing experimentally obtained PSD after sintering with the theoretical predictions can be a route to deduce the sintering mechanism. Observation of Ostwald ripening on model catalyst such as Ge on Si [34], Ag/Ag(110) [35], and Pt/Al_2O_3 [36] model catalysts show a PSD skewed to the left that is in agreement with the Ostwald ripening theory (LSW model). However, Datye et al. argued that none of the sintered industrial-style catalysts exhibit a PSD with a tail towards smaller particles, even for a system

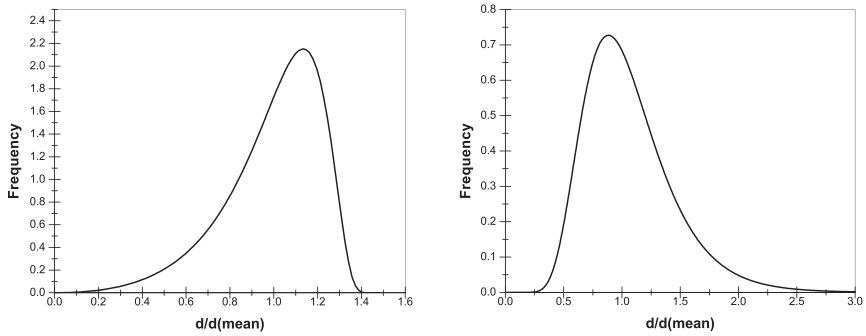

Figure 2.4: Theoretical predictions of particle size distribution of particles after sintering via (left) Ostwald ripening, and (right) particle migration. Reprinted with kind permission from [33].

where Ostwald ripening is favored [37] . Therefore, drawing conclusions on the sintering mechanism by evaluating the PSDs alone is not definitive [37]. Previously, Wanke questioned the use of PSDs for finding the mechanism, by arguing that the PSD of sintered particles strongly depends on the initial size distribution [38]. In Paper 2, we analyze the PSD evolution during oxygen-induced Pt supported on flat silica and alumina where transitional size distributions are observed.

Empirical models were developed to allow better comparison with experimental results, especially when studying sintering at the ensemble level. Two power law expressions (simple and general) have been proposed, which can be applied to both Ostwald ripening and particle migration mechanisms, and possibly predict the sintering mechanism. The first well-known empirical model is the simple power law expression (SPLE) [31]:

$$-\frac{d(D/D_0)}{dt} = k_s(D/D_0)^n \tag{2.3}$$

Where D is the dispersion (the ratio of active surface atoms to total metal atoms), D_0 the initial dispersion, k_s the rate constant, and n is the sintering order. It has been suggested that sintering order, n, can predict the sintering mechanism. Theoretical studies predict n in the range of 3 and 4 for Ostwald ripening [31, 39], while n between 5 and 7 is proposed for particle migration [21, 27, 40, 41]. Experimental

results show that the sintering order may vary from 3 to 15 and is a function of sintering time [3]. It should be noted that the theoretical studies have not taken into account the complexity of the support, which plays a key role in sintering processes. Furthermore, employing SPLE to fit the experimental kinetic data is debatable, as it assumes that dispersion converges to zero after sufficient time. In reality, however, asymptotic dispersion is observed after a long sintering time. By taking the observed asymptotic dispersion into account, the general power law expression (GPLE) [42, 43] can be applied to fit the kinetic data:

$$-\frac{d(D/D_0)}{dt} = k_s(D/D_0 - D_{eq}/D_0)^m \tag{2.4}$$

where D_{eq} is the dispersion at infinite time, and m is the sintering order that is found to be 1 or 2 by fitting to experimental kinetic data on technical catalysts. Using GPLE enables to quantify the correlation between the sintering rate and catalyst properties/sintering conditions [42]. However, no prediction of sintering mechanism was suggested using equation (2.4).

2.3 Experimental techniques to study sintering

Different parameters can be used to quantify the degree of particle sintering, i.e. particle size, distribution and dispersion. Two main approaches can be adopted to study sintering in heterogeneous catalysis. The first is to use model catalyst systems in ultra high vacuum (UHV) as demanded by traditional surface science tools. To study sintering, catalysts can be modeled by depositing metal nanoparticles on flat support (single- or poly-crystalline) [44]. However, real catalysis occurs on complex material systems at high pressures (1 atm or higher), and experimental results from model catalyst in UHV are often quite different from realistic systems and conditions. This is known as material and pressure gap. Great efforts have been dedicated to bridge the material and pressure gap for traditional surface science tools [45–48]. The second approach is the study of real catalysts (e.g. particles dispersed on a mesoporous support) at high pressure (atmospheric pressure or above) and temperature, which offers results comparable to industrial catalysis. In general, operando (i.e. under operating conditions) techniques

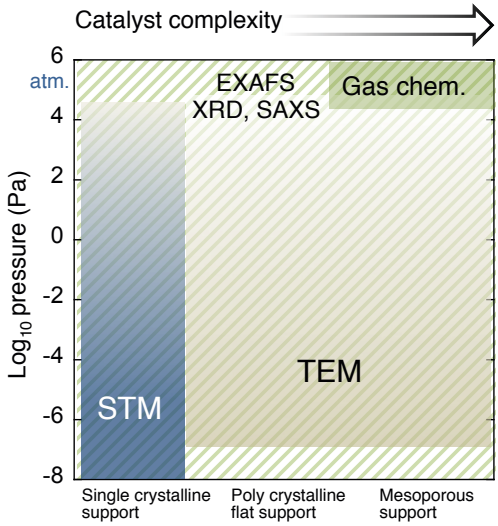

Figure 2.5: Applicability of different techniques to study particle sintering, with respect to the applied pressure and the catalyst complexity.

often lack sufficient surface sensitivity for atom-by-atom characterization, while the surface science approach on model catalyst gives details at the nanoscale but with limited relevance to real catalysis.

Techniques relevant to investigate sintering are discussed below. Figure 2.5 illustrates the applicability of those tools with respect to their typical applied pressure and catalyst type.

Transmission electron microscopy (TEM) is a direct way to estimate the particle size and distribution by imaging the projected area of the particles on the mesoporous or flat support [49]. Besides the projection imaging, the major complication with TEM analysis is that small particles (< 1 nm) might be overlooked due to the low contrast, and it is hard to distinguish overlapping particles. Although TEM does not provide information on the 3D shape of the particles directly, there exist methods to gain such information by, for example, electron tomography [50, 51], and combining scanning TEM (STEM) with other techniques [52, 53] or modeling [54, 55]. In addition, cross-sectional TEM imaging [56–58] can be employed to visualize the nanoparticle/support contact (i.e. the wetting properties of particles on the support) that are important for sintering.

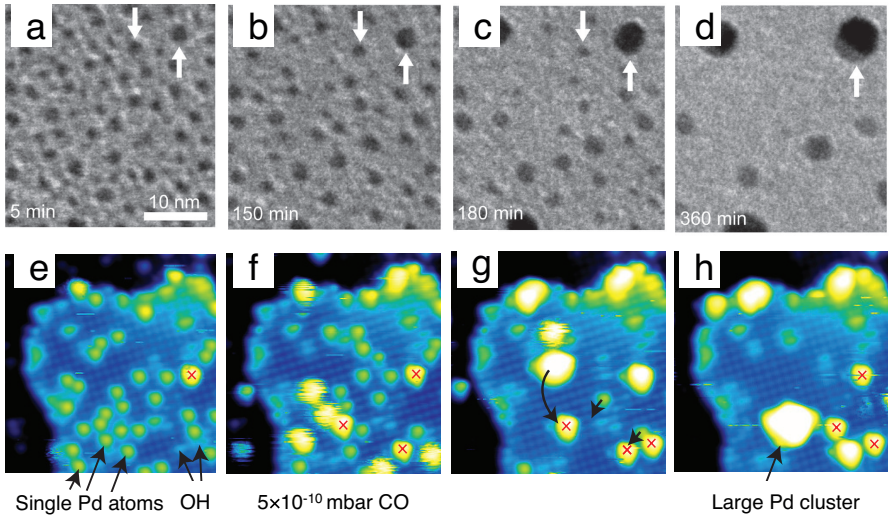

Figure 2.6: Examples of microscopy study to monitor sintering processes (a-d) Time-lapsed TEM images of Pt/Al_2O_3 during exposure to 10 mbar air at 650 °C. Clearly, Ostwald ripening is observed as a dominant sintering mechanism. Modified with permission from [36]. (e-f) Time-lapsed STM images of Pd/Fe_3O_4 during dosing with carbon monoxide at room temperature (time-span = 110 min) shows particle migration and coalescence. Modified with permission from [59].

In recent years, environmental transmission electron microscopy (ETEM) has emerged as one of the most common in situ methods to follow the sintering processes [60]. However, most of those studies have been performed at much lower pressure compared to the realistic catalyst operating conditions [36, 61–66]. An example of in situ TEM studies is shown in Figure 2.6 (top row), where the evolution of Pt particles supported on alumina in 10 mbar air at 650 °C confirms Ostwald ripening as a dominant sintering mechanism. It was shown that by using more sophisticated sample holder design and experimental setup, environmental TEM can be operated at atmospheric pressure [67–71]. Regardless of applied pressure, a possible obstacle associated with TEM is the electron beam damage. Energetic electrons heat the particles locally, which might induce further particle sintering. The practical solution is to reduce the electron current density and carefully investigate the beam effect. On the other hand, some studies exploit the energetic beam to heat the particles locally and follow the dynamical behavior

in situ [72–75] (in these cases, temperature cannot be quantified and imaging is performed in vacuum).

Scanning tunneling microscopy (STM) can be employed to study sintering by obtaining topographic images of particles on a well-defined supports [76, 77]. Design of high pressure (high implies pressures up to mbar range) STM setups has made it possible to study the supported model catalyst in situ [78, 79]. High resolution of STM allows the study of more fundamental surface processes such as monitoring the motion of single adatoms on the support [59]. Figure 2.6 (bottom row) illustrates the formation of large Fe_3O_4-supported Pd clusters by particle migration and coalescence induced by carbon monoxide at room temperature. Such studies are far from realistic catalyst systems and conditions but elucidate surface processes and the role of adsorbates at the nanoscale. One inherent limitation is the inability to perform STM on insulator supports like alumina and silica. In that case, alternative techniques such as atomic force microscopy (AFM) [80–82] can be employed. One should note that if particle size and distribution is of interest, samples with narrow size distribution are more suitable to be studied, ensuring that the analyzed area represents the whole system.

Gas chemisorption measures the amount of gas (e.g. H_2) chemisorbed by the metal on the surface of the support, which can be converted to a metal dispersion by assuming an adsorption stoichiometry [83, 84]. This stoichiometry is defined as the ratio of the number of adsorbed molecules adsorbed per surface metal atom. In hydrogen chemisorption experiments, dispersion is normally determined by assuming the 1:1 ratio of H/Pt. However, unlike TEM where only local information can be obtained, gas chemisorption gives a global surface area value, from which an average particle size can be calculated assuming regular (e.g. spherical) and monodisperse particles.

X-ray diffraction (XRD): Particle size is estimated by considering line broadening of the XRD reflections and applying the so-called Scherrer formula, $D = K\lambda/[Wcos(\theta)]$ [85]. However, very small particles might not be detected and for more precise calculation the Scherrer formula should be modified for specific shape of crystallite and the size distribution [85].

Extended X-ray absorption fine structure (EXAFS) is a syn-

chrotron based technique that estimates not only the size of small particles ($\sim$ 1 nm) at a given temperature and atmosphere, but also the geometric structure of nanoparticles [86, 87]. Another advantage of EXAFS is the possibility to provide chemical information of particles such as detection of adsorbates on nanoparticles and formation of oxide [88, 89] that is important in understanding processes such as sintering [90]. EXAFS is an indirect way to study sintering of particles, where average size and shape of the particles are estimated based on parameters such as average coordination number. EXAFS should be regarded as a complementary method for estimating particles with more than 1200 atoms ($\sim$ 3-4 nm) where in that case accuracy of TEM/XRD is superior [86].

Small angle X-ray scattering (SAXS): In the case of sufficiently homogeneous samples, SAXS can be considered as an appropriate method to provide reliable results based on the evaluation of a large number of particles [85, 91]. SAXS is a photon in-photon out spectroscopy, thus there is almost no constraint on pressure and gas environment. Typically, SAXS requires synchrotron light and could provide time-resolved information [92–94].

Indirect nanoplasmonic sensing (INPS) is an optical spectroscopy method [95] that is further developed in Paper 1 to monitor Pt sintering on alumina and silica support, and in O_2 and NO_2 environment. The detailed description of the technique is provided in section 3.1. INPS enables monitoring of particle sintering under realistic conditions (e.g. atmospheric pressure). High time resolution (of an order of second) signal leads to gain enough information suitable for sintering studies, which might be overlooked by, for example, intermittent TEM imaging. The main constraint is that a complementary method is required to translate the obtained signal to a sintering descriptor (e.g. average diameter or particle density). Nevertheless, simple experimental setup allows for high throughput real time operando measurements of screening type.

Technique	Scale	Catalyst type	Main advantage(s)	Main Limitation(s)
Chemisorption	Global	Model and real	Realistic conditions	Hard to obtain particle size distribution
XRD	Global	Model and real	Realistic conditions	Small particles might be overlooked
SAXS	Global	Model and real	Realistic conditions	Synchrotron is needed
EXAFS	Global	Model and real	Realistic conditions, Shape & chemical Information	Synchrotron is needed, Not precise for particles > ~ 4 nm
TEM	Local	Model and real	Direct way to observe particles	Pressure limitation, Possible beam damage
STM	Local	Model (single-crystal)	Detailed mechanistic view	Pressure limitation, Insulator support cannot be studied
INPS	Global	Model (not single-crystal) and real	Realistic conditions, simple setup	Needs a complementary method to quantify the data

Figure 2.7: Applicability of different techniques to study particle sintering, with respect to the applied pressure and the catalyst complexity.

To conclude, one should note that each tool gives information at different time and length scale. Some has the limitations on the choice of catalyst type and/or the applied sintering conditions. Table 2.7 briefly compares the techniques discussed above.

2.4 Previous studies

In recent decades, several attempts have been made to find the dominant particle sintering mechanism for different catalyst and conditions. The most conclusive way to find the sintering mechanism is to "see" the processes at the particle (or atomic) level using methods such as in situ TEM [60] or time-resolved STM [35, 59]. These studies, despite their detailed mechanistic view, are performed on model catalyst and/or in the low-pressure regime (see Figure 2.6). Another approach is to infer the mechanism from indirect measurements (either ex situ or in situ) by two routes: (1) particle size distribution analysis, and (2) fitting the experimental kinetic data (e.g. change of dispersion over the sintering time) to power-law expressions. The application and validity of these methods are discussed in section 2.2.

Considerable effort has also been put into elucidating the role of several different parameters in sintering of metal particles. These factors in-

clude temperature, metal composition [96], nanoparticle geometry (size [26]/shape [97]) and distribution, interparticle distance [98–100], support, pretreatment, and environment (gas composition and pressure). To compare the results from different studies, one should consider all the experimental details to avoid generalizing the effect of one parameter. The support effect and the gas and temperature environment (relevant to Paper 1 and 2) are briefly reviewed below.

2.4.1 Support effect

Both support morphology and chemistry play a role in sintering of nanoparticles. Particles on mesoporous support are located in the pore structures that make them distant from each other, which hinders the sintering. Moreover, inhomogeneous surface properties such as steps and surface defects (e.g. vacancies) trap the metal species and make them more stable [80]. Beyond the morphology, the chemical nature of a support [101, 102] (e.g. adhesion energy, reducibility, surface defects) also influences the sintering. For example, the stabilizing effect of ceria (CeO_2), which is the oxygen storage component in TWCs, has been shown [103, 104]. In an oxidizing environment, formation of strong Pt-O-Ce bonds could act as anchors that suppress sintering via vapor phase and diffusion of species [105]. The underlying thermodynamic reasons behind the stabilizing effect of ceria was elucidated by Campbell et al [106]. Their calorimetric measurements show larger adhesion energy of Ag to ceria (111) compared to an MgO (100) surface. Moreover, higher amount of oxygen vacancies in ceria (i.e. extent of ceria reduction) increases the metal-oxide adhesion and, thus, more reduced ceria better resists particle sintering [106].

In this thesis, Pt particle sintering on flat amorphous Al_2O_3 and two types of SiO_2 (prepared by different methods) in an oxidizing environment was investigated. Previous attempts to compare Pt sintering on alumina with silica show contradictory conclusions. Compared with alumina, higher [84, 107], comparable [108], and lower [109] degrees of Pt sintering was reported on silica at temperatures above 600 °C in O_2. In general, comparing the supports is a difficult task due to their structural and morphological complexities.

2.4.2 Effect of temperature and gas environment

Particle sintering depends exponentially on the temperature via the Arrhenius expression [3, 42]. Both Ostwald ripening and particle migration involve steps that are affected by the temperature, namely, self-diffusion and detachment of metal atoms (or metal complexes), and diffusion of these species over the support. In Paper 2, the oxygen-induced sintering of Pt/alumina and silica at 500, 550, and 600 °C is studied.

Sintering and redispersion of particles are greatly influenced by the gas environment in the following ways: (a) Formation of metal complexes (e.g. PtO species in an oxidizing environment [41, 110, 111]) influences particle stability by reducing the complex detachment barrier (compared to metal adatom) and/or via desorption of volatile metal complexes. Previous experiments on model catalysts demonstrate enhanced self-diffusion of Pt by hydrogen [112] and Cu by sulfur [113], and more recently CO-induced Pd/Fe_3O_4 sintering [59]. (b) Gas-induced structural change of nanoparticles [56–58, 114–117] could, for instance, change the particle contact angle to the support and subsequently radius of curvature that (according to eq. 2.1) alter the chemical potential and thus influence the sintering processes [118]. The change in the shape of particles under gas conditions can be followed by methods such as EXAFS [86, 87], grazing incidence small angle X-Ray scattering (GISAXS)[57, 119, 120], and in the lower pressure regime (mbar range) environmental TEM [56, 121]. (c) In addition to the adsorbate-induced changes in the nanoparticles, support properties such as structure, chemical state, and defect densities might be altered by gas adsorbates, which in turns influence the stability of the particles [122, 123].

In this thesis, we studied Pt sintering in O_2 and NO_2 environment, and here we focus on oxygen-induced sintering. In an oxidizing environment and at high temperature PtO_x could form [124], however the role of these species with respect to the stability of Pt nanoparticles under different conditions is not clear [125]. For the case of Pt/alumina catalysts in an oxidizing environment, some studies reported redispersion of Pt particles after aging at temperatures below 600 °C on both flat [14, 126–130] and mesoporous support [96, 108, 131–135], while others observed enhanced particle sintering (often) at higher temperatures on flat [36] and high surface area support [42, 133, 134, 136]. It also has

been shown that pretreatment of Pt/alumina in O_2 at temperatures between 400-500 °C has an stabilizing effect [90, 137–139]. One possible route for oxygen-induced particle redispersion is detachment of PtO species followed by migration to the support defects where they get trapped. The surface defects act as nucleation site to generate new particles. Thus, redispersion via this path requires defective support and low metal loading (or large interparticle distances) [129]. On the other hand, oxygen-induced sintering was explained by exchange of volatile PtO_x between the particles (Ostwald ripening through vapor phase), or detachment of PtO species (with lower detachment activation energy compared with Pt) over the support followed by attachment to a neighboring particle [36, 41, 65, 138]. It should be emphasized that several parameters influence the redispersion and sintering processes at the same time. Ouyang et al. theoretically showed that for a given metal and reactant, support material, and reaction conditions (pressure and temperature) play a role in disintegration of metal complexes and possible sintering/redispersion [118].

3

Characterization techniques

3.1 Indirect nanoplasmonic sensing (INPS)

In Paper 1, indirect nanoplasmonic sensing is further estabilished as an operando technique that allows following Pt nanoparticle sintering on different supports and in different gas environments. This section introduces light interaction with metal nanoparticles, and describes how one can use that interaction for sensing purposes. Finally, the applicability of this sensing platform to monitor particle sintering is demonstrated.

Optical properties of metal nanoparticles

Since long time ago, glassmakers have exploited the unusual properties of metal nanoparticles to stain glasses. For example, colloidal suspensions of gold and silver particles produce ruby red and yellow colors, respectively, which differs from their bulk color. Figure 3.1 shows the light transmission through stained glass windows. The first scientific observations of light interaction with small metal particles were made by Faraday [140]. He synthesized colloidal gold particles by reducing gold chloride with phosphorous in water (Figure 3.1 b) and realized that the color of the colloidal solution can be altered by varying the size of its constituent gold particles. The color variation due to the difference in particle size or shape is shown on a state-of-the-art nanofabricated sample in Figure 3.1 c.

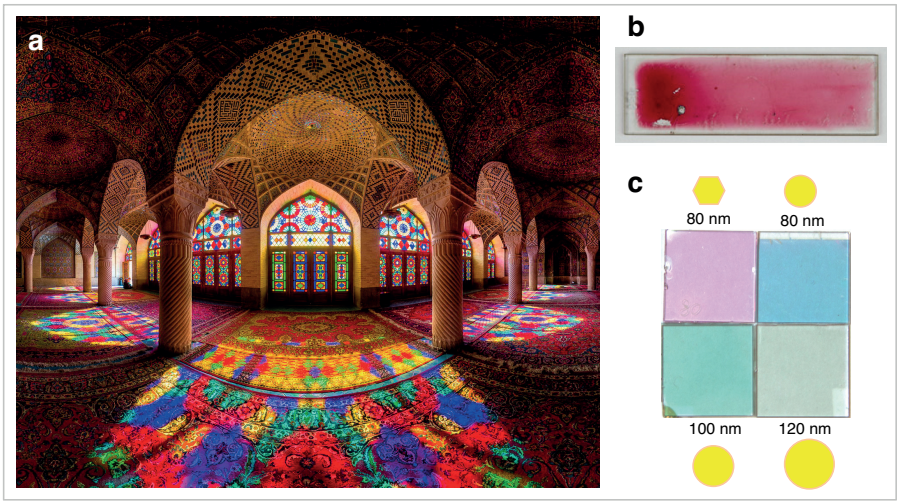

Figure 3.1: (a) Light shines through stained glass windows in the Pink Mosque located in Shiraz, Iran. Photo courtesy of Mohammad Reza Domiri Ganji. (b) Gold colloids on a microscope slide that was prepared by Faraday. Copyright of Whipple Museum of the History of Science. (c) Gold particles with different size/shape nanofabricated on a glass substrate.

When light shines on a metal particle of a size comparable to the wavelength of light, the conduction electrons of that particle can oscillate collectively in resonance with the incoming light frequency – this is called localized surface plasmon resonance, LSPR [141] (Figure 3.2 a). The LSPR has two consequences of relevance for the work presented in this thesis, namely the appearance of a peak at a specific wavelength, λ_p, in the optical far field extinction (sum of scattering and absorption) spectra (Figure 3.2 b), and an enhanced electromagnetic near field around the particle (Figure 3.2 c). If the plasmon peak wavelength lies in the visible region of the electromagnetic spectrum, parts of irradiated white light are absorbed and scattered by the particle, which leads to the coloration effect that is seen in Figure 3.1. The spectral position of the plasmon peak (i.e. the resonance frequency of the collective electron oscillation) depends on the composition, the shape and size of the particle, as well as the dielectric environment around the particle. The latter is a basis of nanoplasmonic sensing that is described in the following.

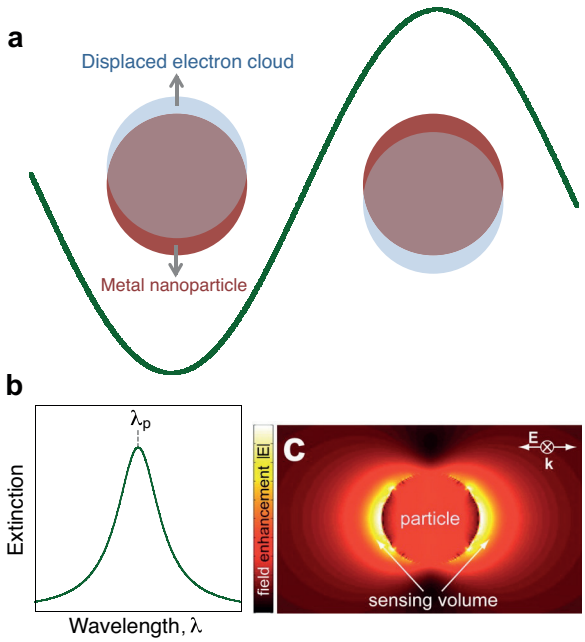

Figure 3.2: (a) Light with appropriate wavelength can excite the free electrons of a metal nanoparticle, and cause them to oscillate coherently in resonance with external field. This resonance gives rise to two effects: (b) a distinct peak in far field extinction spectra at the resonance wavelength, λ_p, that results from strong scattering and absorption of light, and (c) an enhanced electromagnetic near field around the particle. Field enhancement around a gold nanodisk (diameter = 80 nm and height = 20 nm) illuminated at the LSPR wavelength as simulated by the finite-difference time-domain (FDTD) electrodynamic simulation method. Panel c is reprinted with permission from [95]. Copyright 2012 American Chemical Society.

Nanoplasmonic sensing

The dependence of the plasmon peak wavelength (λ_p) of a small spherical particle on the refractive index of the medium, n, is expressed by

$$\lambda_p = \lambda_b \sqrt{2n^2 + 1} \tag{3.1}$$

where λ_b is the bulk plasmon wavelength of the material. Figure 3.3

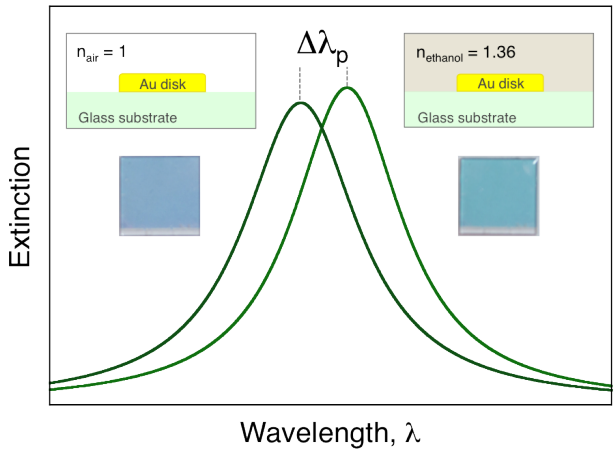

Figure 3.3: Basic principle of nanoplasmonic sensing. The sample to the left shows the ensemble of gold nanodisks (diameter $\simeq$ 80 nm and height $\simeq$ 20 nm) on a glass substrate in air, whereas to the right, the same sample is covered by ethanol. Because of the change in the refractive index around the particles, the plasmon peak is shifted and causes color change (see equation 3.1). This sensitivity towards refractive index changes is the basis of nanoplasmonic sensing. In this example, the spectral shift is large enough that can be observed by eye.

demonstrates the color change of gold nanoparticles illuminated with white light after pipetting a few drops of ethanol onto them. The reason is that, according to equation (3.1), varying the refractive index around the particles leads to the shift in plasmon peak wavelength, and consequently the change in color. This dependency allows plasmonic particles to "sense" the local changes in refractive index of their surrounding. In nanoplasmonic sensing the readout is often a spectral shift of the peak wavelength (λ_p) that can be measured by a spectrometer with high temporal and spectral resolution. Nanoplasmonic sensing has been employed in biological analyte detection [142, 143], as well as in materials science [144–146], including catalysis studies [95]. Among many plasmonic metals, gold and silver are generally chosen thanks to their suitable dielectric properties (low losses in the visible spectral range). In this context, it should be noted that the plasmonic sensor nanoparticle can detect the refractive index changes only within a limited region (extending a few tens of nanometers from the particle

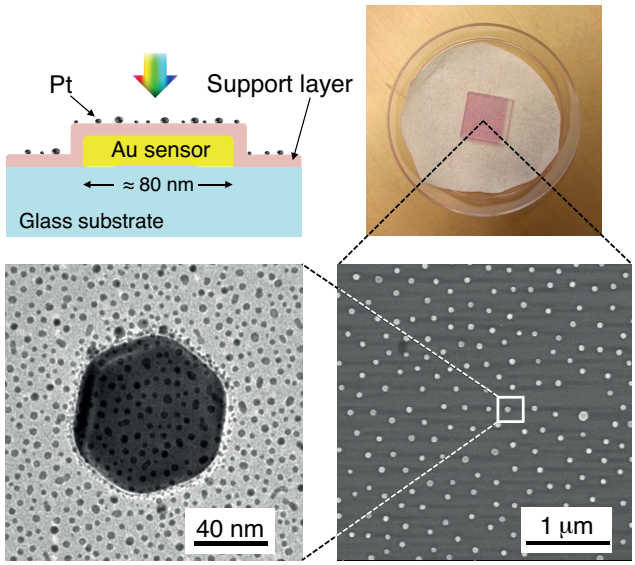

Figure 3.4: Indirect nanoplasmonic sensor. (Top left) The INPS sensor consists of an array of Au nanoparticles fabricated on a glass substrate. They are covered by a thin layer of oxidic catalyst support material, on which the Pt particles are deposited. (Top right) 1×1 cm INPS sensor. (Bottom right) Environmental SEM image of plasmonic gold sensor nanoparticles covered with a 10 nm thick silica catalyst support layer. (Bottom left) TEM image of as-deposited Pt on a single gold sensor nanoparticle covered with a 10 nm thick silica catalyst support layer.

surface), which in most cases is advantageous. This region is called the sensing volume, and it corresponds to the enhanced electromagnetic field around the particle (Figure 3.2 c). The specifics of the field enhancement and similarly the sensing volume depend on the metal, particle geometry, and the dielectric environment of particle.

To monitor nanoparticle sintering in situ, the plasmonic sensing described above can be performed indirectly, i.e. by depositing an oxide spacer layer between the arrays of plasmonic gold nanosensors (diameter $\simeq$ 80 nm, height $\simeq$ 20 nm) and the catalyst nanoparticles to be probed (Figure 3.4). This specific sensing platform is referred to as indirect nanoplasmonic sensing (INPS) [144]. The oxide layer serves as a support material for the catalyst particles and provides additional important functions: (a) to protect the gold particles from harsh gaseous

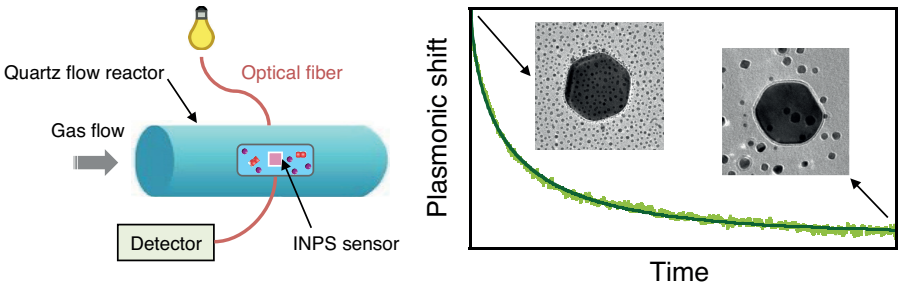

Figure 3.5: (Left) Schematic of the INPS setup; the INPS sensor decorated with Pt particles is exposed to the desired gas environment at high temperature in a quartz flow reactor, through which the optical extinction measurement is performed. (Right) Plasmonic peak shift reflecting the sintering of Pt nanoparticles on the INPS sensor. The TEM images show a single gold sensor with Pt before exposure to 4% O_2 in Ar at 600 °C, and after 12 h in the gas mixture. The dimensions of TEM images are 160 × 160 nm^2.

environment, and (b) to prevent alloying between the catalyst particles (e.g. Pt) and the gold sensors at high temperature.

The INPS setup (Insplorion X1 flow reactor system, Insplorion AB, Göteborg, Sweden) consists of a quartz flow reactor with optical access for transmission measurement, and is equipped with a heating coil and mass flow controllers to provide the desired operating conditions (Figure 3.5 left). The INPS sensor with the deposited Pt is placed in the reactor, and is then exposed to the sintering temperature and desired gas conditions. Rearrangement of the Pt particles due to sintering changes the effective refractive index around the sensor gold particles below and, hence, causes a shift in the plasmon peak (λ_p). The spectra are recorded by a spectrometer with high temporal resolution to obtain operando high-resolution kinetic data (Figure 3.5 right). The TEM images in the plot show the Pt particles on a gold sensor before exposure to the sintering conditions, and after 12 h of sintering. Clearly, the mean particle size increases in general agreement with the INPS measurement.

Note that the plasmonic signal, i.e. the spectral shift of the peak wavelength, does not directly express the extent of sintering quantitatively. Thus, the experimentally measured plasmonic signal has to be converted

to a sintering descriptor such as mean particle diameter, $\langle D \rangle$ [147]. To do that, TEM is performed to determine the mean diameter of sintered particles after certain time intervals, which is then correlated to the measured plasmon peak shift after the same time intervals. Following this procedure, the plasmon peak shift, p, (e.g., in Figure 3.5 right) can be "translated" to the mean particle size by an empirical calibration formula that relates λ_p to $\langle D \rangle$ (details are provided in Paper 1). By this translation, high (temporal) resolution quantitative kinetic data of the sintering process is obtained under realistic conditions and can be considered for further analysis.

In Paper 1, we mainly demonstrates the applicability of INPS to monitor sintering in operando with considerable flexibility in the choice of catalyst support material and gas environments. To find the Pt sintering kinetics at 600 °C on different supports and in different gas environments INPS complements with ex situ TEM analysis. Three different conditions are investigated, namely, Pt/silica in 4% O_2 in Ar, Pt/alumina in 4% O_2 in Ar, and Pt/silica in 0.1% NO_2 in Ar.

3.2 Transmission electron microscopy (TEM)

Similar to the optical microscope, the transmission electron microscope (TEM) [148] forms the two-dimensional image of the sample. The main difference is that instead of visible light, in electron microscopy accelerated electrons with much shorter wavelength are utilized to achieve higher resolution. According to the de Broglie equation, $\lambda = h/p$ (h is Planck constant and p is the electron momentum), electrons with higher energy have shorter wavelength that enables microscopy with greater resolution. Thus, to ultimately reach the atomic resolution, the electron beam is typically accelerated with 80 kV to 300 kV voltage. Due to strong electron-sample interaction, the sample should be thin enough (below 100 nm) for electron transmission. In this study, supported Pt particles are deposited on a 40 nm thin Si_3N_4 membrane (see section 4.4).

Figure 3.6 shows the schematic illustration of a TEM setup that consists of the electron source, the imaging system (lenses), and a display system. Two kinds of electron sources are used; thermionic and field emission. Thermionic sources are made from a material with high melt-

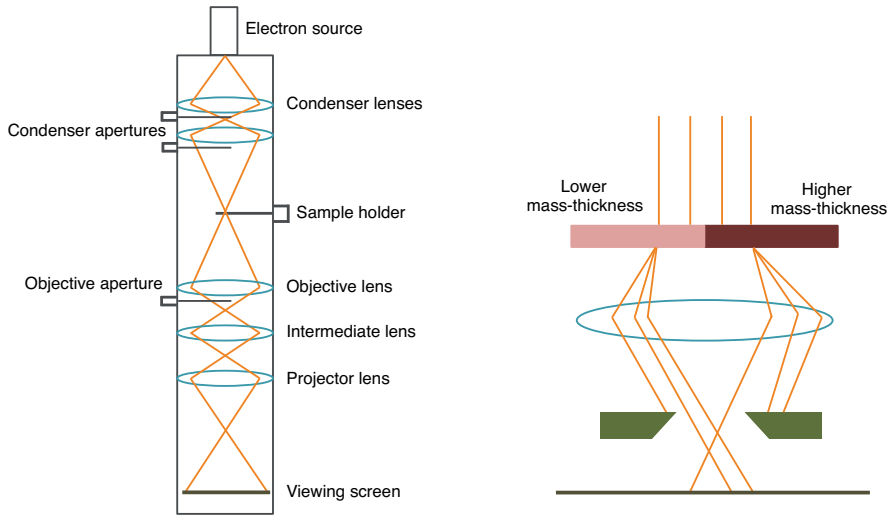

Figure 3.6: Schematic illustration of (right) TEM and a simple ray diagram showing how the image is formed, and (left) scattering of incident electron beam by regions with different mass-thicknesses. Adapted from [148].

ing point and low work function that produces electrons by heating it, whereas in a field-emission source, a large electric potential between the source (e.g. tungsten) and an anode creates electrons. The TEM used in the present study employs LaB_6 crystals as thermionic source. The imaging system mainly consists of electromagnetic lenses (that can be considered as convex lenses) and apertures. The first condenser lens demagnifies the crossover to a smaller spot size and the second lens enlarges this spot size. The condenser lens thus controls the amount of electron radiation illuminating the sample. The objective lens that is placed after the sample is used to focus and initially magnify the image. Further magnification is performed by the intermediate and the projector lenses. The display system is a florescent screen that detects the transmitted electrons as well as a CCD camera. In this work, TEM (FEI Tecnai G2 T20) imaging was performed in the bright-field mode where the contrast mainly arises from the diffraction-contrast and mass-thickness of the sample at the applied magnifications. Figure 3.6 (right) illustrates how incident electron beam scattered by the regions with different mass-thicknesses. The region with higher mass-thickness scatters the electron beam more strongly, hence a weaker beam is passed through the aperture and they appear darker. For this reason, Pt par-

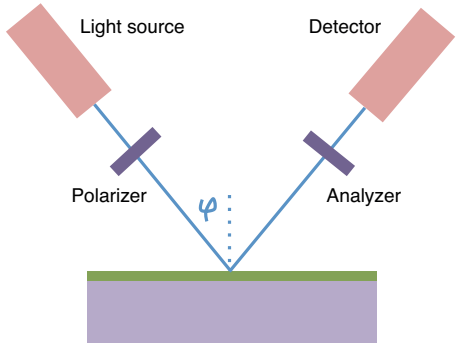

Figure 3.7: Schematic picture showing the principle of ellipsometry.

ticles appear darker compared with alumina or silica support.

3.3 Ellipsometry

In Paper 1, ellipsometry (J.A. Woollam M-2000) is performed to determine the refractive index of the support material (i.e. spacer layer of the INPS sensors). Figure 3.7 shows the simple schematic of the setup. The linearly polarized light is shone on the sample, and becomes elliptically polarized upon reflection. The reflected light passes through the rotating polarizer (i.e. analyzer) and reaches the detector where the amount of polarization, both in amplitude and phase, is determined. The change in polarization depends on several sample properties, such as composition, refractive index, and thickness. By providing an estimate of the layer thickness, the refractive index is obtained through fitting to optical models.

In this work, we deposit 50 nm-thick sputtered alumina and PECVD silica layer on a silicon substrate that is followed by 36 hours heat treatment at 615 °C. A thicker layer compared to the support layer on the sensor (10 nm) is deposited for these measurements to eliminate the effect of interface layer between silicon substrate and the oxide [149].

4 Sample fabrication

In this thesis, supported Pt particles are deposited on either gold sensors or TEM windows. This chapter describes the fabrication of gold sensors and deposition of support material, as well as evaporation of Pt particles. At last, the structure of TEM window is described.

4.1 Fabrication of gold sensors

In Paper 1, gold sensors in the form of disks (diameter $\approx$ 80 nm, height = 20 nm) are fabricated on the glass substrate, using hole-mask colloidal lithography (HCL) [150], followed by gold deposition. HCL is a bottom-up nanolithography method that is based on the self-assembly of charged polystyrene particles to produce the hole-mask. The sensors are fabricated in the MC2 cleanroom at Chalmers. The different process steps (Figure 4.1) are explained below.

(a) The process starts with spin coating of the clean glass substrate with a thin Polymethyl methacrylate (PMMA) layer ($\sim$100 nm), followed by 10 minute hot plate baking at 170 °C to evaporate excessive solvent. To make the surface hydrophilic for the next steps, the sample is treated in oxygen plasma for five seconds (ashing). Polydiallyldimethylammonium chloride (PDDA) diluted to 2 % in deionized water are pipetted to charge the surface positively, followed by rinsing with deionized water

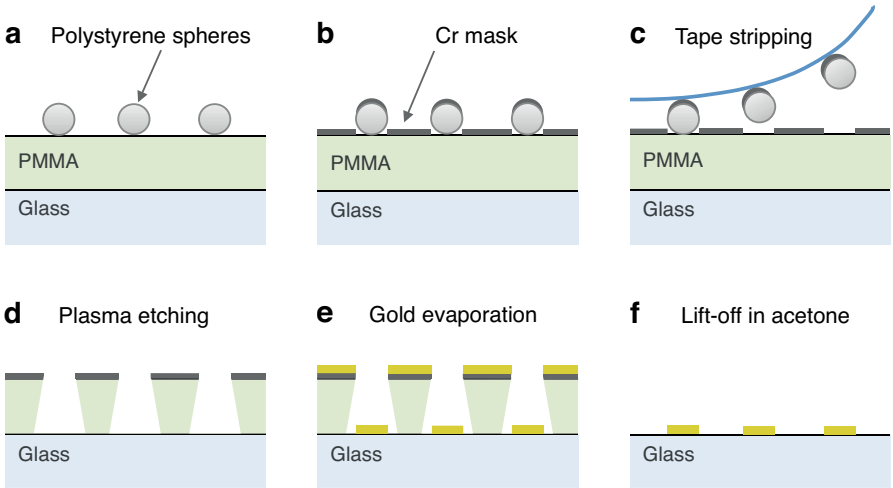

Figure 4.1: Steps in the fabrication of gold nanodisks. (a-d) hole-mask colloidal lithography produces a mask through which (e) gold is evaporated, and finally (f) the residue layers are removed. See the text for explanation of each step.

and nitrogen blow-drying. Thereafter, negatively charged polystyrene (PS) colloids diluted to 0.2 % in deionized water are pipetted on the surface (about 1 minute waiting time), followed by rinsing and blow-drying. Since the surface and PS particles have opposite charges, PS particles stick to the surface and maintain some distance by repelling each other. The result is a quasi-random arrangement of particles on the surface. The density of particles on the surface can be tuned by the PS colloid concentration, while the interparticle distances can be increased by adding salt (e.g. NaCl) to the colloidal solution. The average diameter of PS particles in our work was about 80 nm.

(b) The metallic mask (e.g. 20 nm chromium) is evaporated on the sample surface by a Lesker evaporator. The basic principle of e-beam evaporation is described in section 4.3.

(c) The polystyrene particles can be removed by tape stripping. This leaves arrays of circular holes on the PMMA surface.

(d) The last step in producing the mask is to etch through the holes. By oxygen plasma etching, reactive components chemically react with PMMA and form volatile compounds, where the (Cr) mask remains

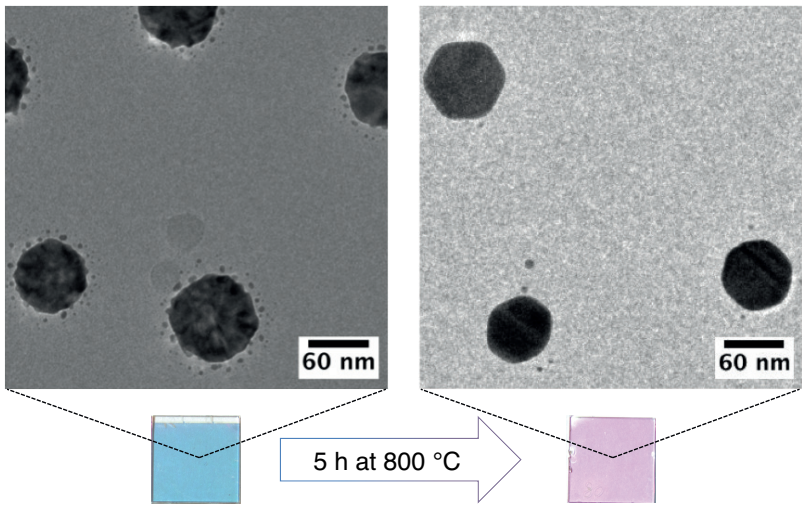

Figure 4.2: Gold particles are heat treated to become stable. TEM image and the corresponding sensor chip shows gold particles (Left) as prepared, and (right) after 5 hours heat treatment at 800 °C.

intact. The amount of undercut (see Figure 4.1 d) can be changed by the etching time. Our samples were etched for 3 minutes at this stage.

(e) A gold film of 20 nm thickness is thermally evaporated (using Lesker evaporator). Evaporation is a directional deposition method, thus gold nanodisks with average diameter of about 80 nm (size of holes in the mask) and height of 20 nm are formed on the glass substrate without any contact to the PMMA (see the figure).

(f) In the last step, the PMMA layer and the deposited layers on top are lifted-off in acetone, leaving only the gold nanodisks (i.e. sensor particles) on the surface.

Gold particles are then heat treated to assure that their shapes are retained during high temperature experiments (note that the change in the particle shape induces a spectral shift in INPS measurements). Figure 4.2 shows the effect of heat treatment (5 hours at 800 °C) on the gold nanodisks where they become faceted and attain hexagonal shape. Upon the shape change, the plasmon peak wavelength of particles is notably shifted, which can be seen from the gold color after the heat treatment.

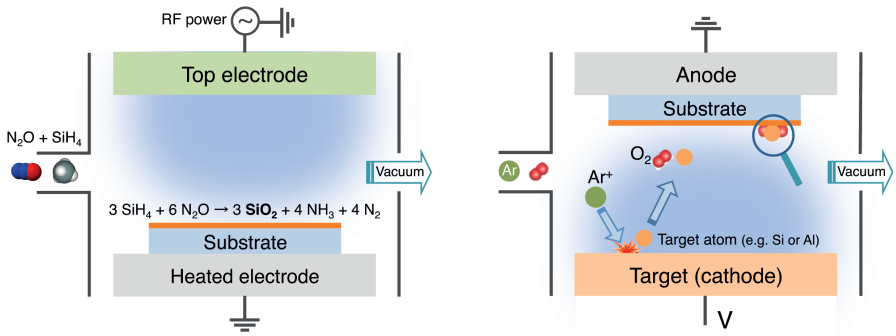

Figure 4.3: Schematic of (Left) plasma-enhanced chemical vapor deposition (PECVD) of silica, and (right) reactive sputter deposition of silica or alumina.

4.2 Deposition of support materials

Flat supports were deposited on gold sensors (Paper 1) and TEM windows (Paper 1 and 2) by means of sputtering and plasma-enhanced chemical vapor deposition (PECVD) that are explained below. Support layers are then heat treated for 36 hours at 615 °C to become stabilized (e.g. in terms of density and RI) for INPS measurements.

Plasma-enhanced chemical vapor deposition

In general, chemical vapor deposition uses chemical processes to produce conformal thin films (i.e. no thickness variation along edges, steps, etc.). The substrate is exposed to the reactants (gas precursors) where the material of interest is chemically formed on the surface. In PECVD, the plasma produces energetic species that assist the gas phase reactions, hence, it becomes possible to deposit at low temperature (between 200 °C and 400 °C) compared with thermal CVD. To create the plasma the reactant gases are introduced between two parallel electrodes. The heated electrode that supports the substrate is electrically grounded, while RF (radio frequency) power is applied to the top electrode (Figure 4.3 left). In this work, SiO_2 is deposited by PECVD (STS) using silane (SiH_4) and nitrous oxide (N_2O) as silicon and oxygen precursor, respectively.

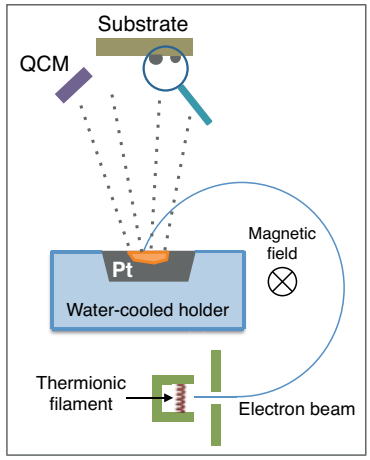

Figure 4.4: Basic principle of electron-beam evaporation of platinum.

Sputter deposition

Sputter deposition is a physical vapor deposition (PVD) method that was used in this thesis to deposit alumina and silica. The schematic of the technique is shown in Figure 4.3 (right). An inert gas such as argon is introduced to the chamber, and the plasma (including Ar ions) is created by applying DC or RF voltage between two electrodes. Energetic positive Ar ions are attracted to the cathode that is a target material (e.g. Al or Si). The collisions between Ar ions and target material eject the target atoms. This process is referred to as sputtering. The sputtered atoms move in all directions and could then hit the substrate. To deposit silica and alumina (compound materials), reactive sputter deposition is used where oxygen that is fed into the chamber reacts with the sputtered Al or Si atoms to form the oxides. In the present study, silica and alumina were deposited by an FHR MS 150 machine.

4.3 Growth of Pt nanoparticles

In this thesis, Pt nanoparticles are grown by electron beam evaporation (AVAC HVC600 evaporator). To heat the target material (Pt), emitted electrons from the hot filament are accelerated (accelerating voltage of 3 to 40 kV), and directed to the Pt source with the help of a magnetic field (Figure 4.4). Since evaporation is carried out in a vac-

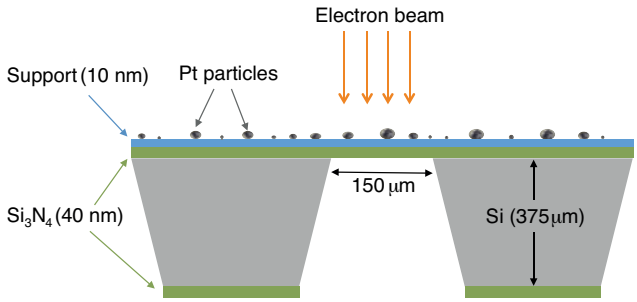

Figure 4.5: Schematic of TEM window, on which support material and Pt particles are evaporated. Note that the dimensions are not to scale. Adapted from [151].

uum chamber, the Pt atoms (in vapor phase) travel within line of sight and finally condense on the substrate. The holder is water-cooled to avoid contamination that might result from evaporation of the holder material. The thickness of the deposited layer is monitored by quartz crystal microbalance (QCM), while the electron beam current controls the deposition rate. In our experiments, nominally 0.5 nm thick Pt was deposited at the rate of 0.5 Å/s, which results in the formation of nanoparticles (island growth mode) with average diameter of about 3 nm.

4.4 TEM samples

To perform TEM, support material and subsequently Pt particles are deposited on TEM "windows" that consist of an 40 nm electron-transparent amorphous Si_3N_4 membrane [151]. The TEM windows in this study have been fabricated in the MC2 cleanroom at Chalmers by the different steps including growth of Si_3N_4, pattering by photolithography, and chemical etching of silicon. The structure of such TEM windows is illustrated in Figure 4.5. The thickness of membrane influences the resolution of the imaging due to diffuse scattering of electrons by the nitride layer. The silicon nitride thickness in our windows is 40 nm that adds notable weight to the background mass-thickness. Therefore, it is difficult to estimate the size of small Pt particle (< 1 nm) due to inadequate contrast with respect to the beneath layers, namely, 10 nm support material and 40 nm silicon nitride membrane.

5

Summary of sintering studies

In Paper 1, indirect nanoplasmonic sensing (INPS) was further established and tested as as an operando tool that in combination with TEM allows the monitoring of Pt sintering on different supports and under different gas conditions with high time resolution. The principle behind INPS is that the position of the plasmon peak of the gold particles (i.e. sensors) is sensitive to changes in the dielectric environment, in this case the rearrangement of Pt nanoparticles. Previously, INPS has been used to explore sintering of Pt/SiO_2 in O_2 environment in a proof-of-principle study [147]. Here, the flexibility of INPS to follow Pt sintering on different supports and under different gas conditions was demonstrated for the first time. Three different sintering experiments at 600 °C were considered, namely, Pt/Al_2O_3 in 4 % O_2, Pt/SiO_2 in 4 % O_2, and Pt/SiO_2 in 0.1 % NO_2. To understand and account for the role of the support refractive index in the measured INPS signal, finite-difference time-domain (FDTD) electrodynamics simulations of the structures were performed, where a linear relation between the change in the INPS signal and the support refractive index (RI) was found. This enabled comparison of the Pt sintering on different supports by scaling the data with refractive index of the support.

Figure 5.1a shows the RI-scaled change in the INPS signal (i.e. centroid position) due to exposure of Pt particles to O_2 and NO_2 gases. The blank sensors (i.e. without Pt) do not exhibit significant shift dur-

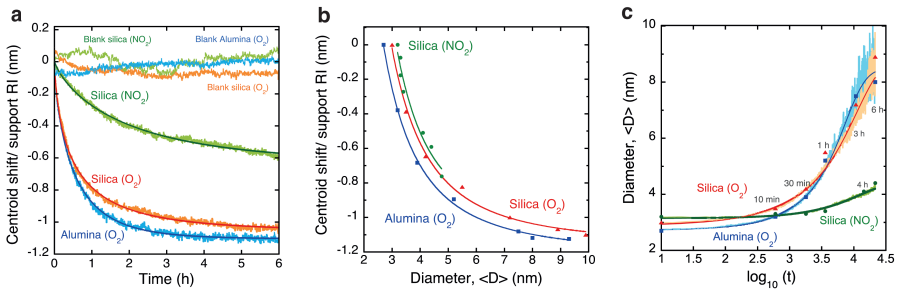

Figure 5.1: (a) INPS sintering curves scaled with the refractive index of the support layer. The solid lines correspond to an exponential function fitted to the raw INPS curves. Corresponding INPS traces of blank sensors (i.e. without Pt) exhibit a negligible centroid shift at the applied conditions. (b) Correlation between refractive index-scaled INPS centroid signal and mean particle diameter, $\langle D \rangle$. Calibration formula is obtained by fitting a function of a form $\lambda_p = \mathrm{A} + \mathrm{B}\ \langle D \rangle^{-n}$ to the experimental points. (c) High resolution real time sintering kinetic data (solid lines) obtained by translating the centroid shift to mean particle size, $\langle D \rangle$, using the derived translation functions from the analysis in panel (b). The dark full lines correspond to fitted exponential functions to the raw data and serve as a guide to the eye. The discrete points show the mean particle diameter derived from TEM.

ing the same conditions. In order to relate the measured INPS signal to a sintering descriptor such as mean particle diameter, TEM analysis of sintered particles were performed at certain time intervals. Each discrete point in Figure 5.1 b shows the mean particle size after designated time intervals and the corresponding RI-scaled centroid shift. Fitting of a function of the form $\lambda_p = \mathrm{A} + \mathrm{B}\ \langle D \rangle^{-n}$ to the experimental points yields an empirical calibration formula to "translate" the real time INPS data (i.e. plasmon peak shift) to the real time evolution of the mean particle diameter. This translation allows deducing real time high-resolution kinetic data for the three cases studied (Figure 5.1 c). The results show comparable degrees of Pt sintering on both alumina and silica support in 4 % O_2 and noticeably less sintering of Pt on silica in 0.1 % NO_2. However, one should note that the gas partial pressure (i.e. concentration) influences the sintering processes, and drawing conclusion on the specific role of O_2 and NO_2 in Pt sintering cannot be made by the present data.

In conclusion, INPS employs a relatively simple setup to screen the par-

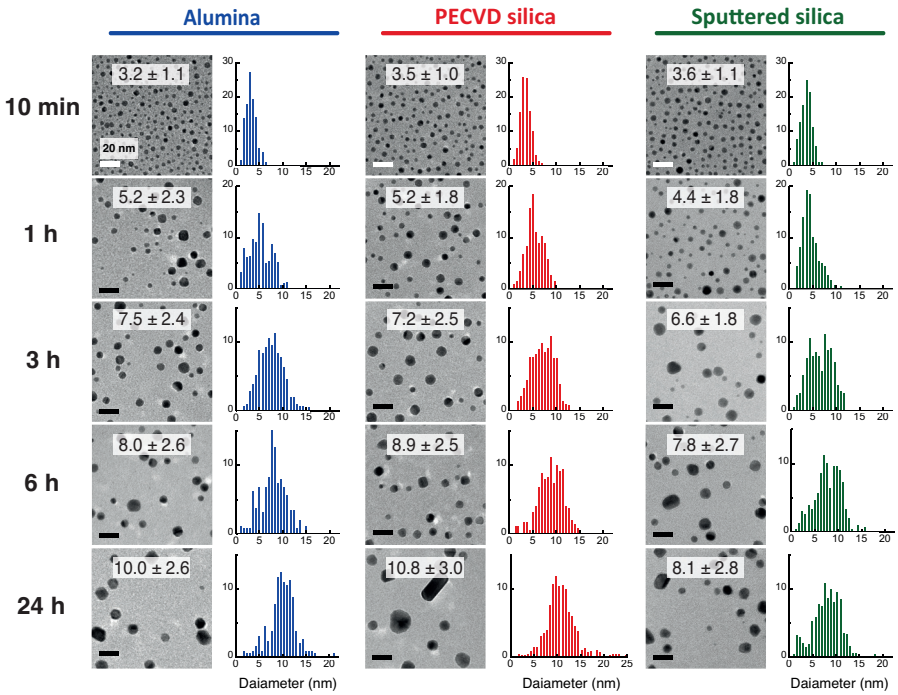

Figure 5.2: TEM images and corresponding particle size distribution of Pt particles supported on alumina, PECVD silica, and sputtered silica during sintering in 4 % O_2 at 600 °C after different time intervals The mean diameter and standard deviation is written on each TEM image. The scale bar in all images represents 20 nm. The x axis in the histograms shows the frequency of particles within each bin size.

ticle sintering at the ensemble level with high time resolution and under realistic conditions. One complication regarding the INPS is that the signal is not selectively sensitive to the rearrangement of particles, and other processes that change the dielectric environment around the sensors give rise to the signal shift. Therefore, careful design of experiment to rule out other possible events that results to the plasmon peak shift is crucial. Nevertheless, the high throughput INPS platform offers a possibility to compare the sintering kinetics by varying one experimental parameter (e.g. gas partial pressure) as the same calibration formula is expected to be valid for the same catalyst system.

As mentioned, the kinetic data obtained by INPS (Paper 1) are based

on ensemble average of particles, and some information on evolution of particles during sintering might be overlooked. To elucidate the sintering processes in more detail the particle size distributions (PSDs) of Pt particles on alumina, PECVD silica, and sputtered silica were analyzed during sintering for up to 24 hours at 600 °C (time-resolved), and after 12 hours at 500, 550, and 600 °C (temperature-resolved) in 4 % O_2 in Ar. The two types of silica that were deposited by different methods differ from each other in terms of stoichiometry and probably also surface roughness. The ongoing characterization of the supports will aid the interpretation of their properties.

Figure 5.2 shows some of the time-resolved TEM images and corresponding PSDs. The initial PSDs (before exposure to oxygen) for all the cases are Gaussian with a peak centered around 3 nm. Transitional bimodal distributions are observed for Pt sintering on all three supports, which are not in match with the conventional theoretical predictions of sintered particle size distributions. Theoretical calculations considering local support heterogeneity will be performed to explain these findings. The observations did not imply any significant difference for oxygen-induced Pt sintering on alumina and two types of silica. However, a lower onset temperature for Pt sintering on both silica supports compared with alumina was recorded.

In paper 2, the difficulty of deducing the dominant sintering mechanism (i.e. atomic migration or particle migration) from either particle size distribution of sintered particles or fitting the kinetic data with the simple power law equation was highlighted. Therefore, the only conclusive way to find the sintering mechanism is a direct visualization at particle/atomic level under realistic conditions. Future advances in techniques, such as environmental TEM, could open doors to that direction.

6 Conclusions and outlook

This thesis explores the oxygen-induced sintering of Pt nanoparticles on silica and alumina at atmospheric pressure. In Paper 1, the applicability of INPS and TEM to obtain high resolution Pt sintering kinetics on different support materials (silica and alumina) and in O_2 and NO_2 environments was demonstrated. In Paper 2, the evolution of the Pt particle size distribution during sintering in O_2 as a function of time and temperature was analyzed.

In the future, many interesting ideas could be explored to further elucidate the Pt sintering under operating conditions and optimize the INPS platform for sintering studies. For example, the relationship between the INPS signal and the details of rearrangement of particles is not yet well understood. Theoretical simulations of changes in Pt particles on individual sensor particles can help to clarify this relationship, which in turn will help to better interpret the INPS data in a quantitative fashion. One way to validate the simulation results could be to exploit the INPS platform at the single gold particle level, in contrast to the present study where arrays of gold sensor particles were used.

One possibility to extend the application of INPS for sintering studies is to apply the technique to particles dispersed on high surface area oxide that resembles the technical catalysts. This can be achieved, for example, by conventional wet chemistry to prepare the catalyst and spin coating of oxide slurry on an INPS sensor chip. In this way, a step

closer to real catalyst systems could be taken.

A more ambitious outlook could be to combine INPS with other operando spectroscopic techniques such as EXAFS to acquire more information on, for example, the chemical state of particles/support during sintering processes.

7 Acknowledgments

This work was funded by and performed at the Competence Centre for Catalysis, which is hosted by Chalmers University of Technology, and financially supported by the Swedish Energy Agency, and the member companies: AB Volvo, ECAPS AB, Haldor Topsøe A/S, Scania CV AB, Volvo Car Corporation AB, and Wärtsilä Finland Oy.

The studied samples were fabricated at the MC2 nanofabrication laboratory at Chalmers University of Technology.

First of all, I would like to express my gratitude to my supervisors Henrik Grönbeck and Christoph Langhammer for their remarkable supports that made it possible to accomplish this thesis.

Henrik Grönbeck, your dedication to science has always been an inspiration for me. I appreciate all the time you put for me despite your busy schedule. I also greatly appreciate your effort on carefully reading this thesis, which made it much improved from its early stages.

Christoph Langhammer, I am grateful to have you as my co-supervisor as I feel that I have a second main supervisor. During all the discussions, you always encouraged me by providing great ideas and solutions.

I would also like to thank the following people:

Magnus Skoglundh, for giving me the opportunity to start my work at KCK, and all the helpful discussions on my project.

Igor Zorić, for being the one who first made me interested in the field of plasmonics (already in the interview), and also for reviewing my thesis.

Vladimir Zhdanov, for all the fruitful discussions and collaboration on the second paper.

Tomasz Antosiewicz, for performing the FDTD simulations, and **Franceco Mazzotta**, for the additional experiments in Paper 1.

Torben Pingel, for teaching me to operate Tecnai TEM, and also all the fun time outside Chalmers.

All the current and former members of Chemical Physics for their support inside and outside the lab, especially the following people: **Elin Larsson**, for all the help with the lab works in the beginning of my project, **Carl**, for coaching me to operate the cleanroom tools, **Viktoria**, for helping me with ellipsometry, **Ferry**, for taking nice photos of my samples, and **Farzin** for always sharing interesting ideas. And of course, my current and former office mates, **Kristina**, **Beniamino**, **Anna**, **Raja**, and **Viktor** for bringing a nice atmosphere to the workplace, and all the small and big helps. People who made the lunch time more interesting, especially **Maxime** and **Deborah** (actually from Biological Physics).

Biological Physics, and Bionanophtonics group members who share the kitchen with us, and making a friendly working atmosphere. Special thanks to **Mokhtar** for always being a nice friend, and helping me with the idea of nanofabrication on thin membranes.

Members of KCK, especially those who have accompanied me during the Denmark summer school and NAM conference, and making those events more fun.

I owe my parents a lot, for all their supports and encouragements during the past decades.

And last but not least, I would like to say a big thanks to **Anahid** for all the love, support, and friendship during these years.

Bibliography

[1] IARC Working Group on the Evaluation of Carcinogenic Risks to humans, *Diesel and gasoline engine exhausts and some nitroarenes*, vol. 105 (International Agency for Research on Cancer (IARC), 2012).

[2] *Regulation (EC) No 715/2007 of the European Parliament and of the Council* (2007).

[3] C. H. Bartholomew, Applied Catalysis A: General **212**, 17 (2001).

[4] M. Saurat and S. Bringezu, Journal of Industrial Ecology **12**, 754 (2008).

[5] *The components of autocatalyst demand*, Johnson Matthey Company (2013).

[6] A. Cao, R. Lu, and G. Veser, Physical Chemistry Chemical Physics **12**, 13499 (2010).

[7] I. Chorkendorff and J. W. Niemantsverdriet, *Concepts of Modern Catalysis and Kinetics* (Wiley-VCH, 2007), 2nd ed.

[8] M. Valden, Science **281**, 1647 (1998).

[9] M. S. Chen and D. W. Goodman, Science (New York, N.Y.) **306**, 252 (2004).

[10] A. T. Bell, Science (New York, N.Y.) **299**, 1688 (2003).

[11] A. Russell and W. S. Epling, Catalysis Reviews **53**, 337 (2011).

[12] R. M. Heck, R. J. Farrauto, and S. T. Gulati, *Catalytic Air Pollution Control: Commercial Technology* (John Wiley & Sons, 2009), 3rd ed.

[13] M. Skoglundh and E. Fridell, Topics in Catalysis **28**, 79 (2004).

[14] R. Gollob and D. Dadyburjor, Journal of Catalysis **68**, 473 (1981).

[15] F. Le Normand, A. Borgna, T. F. Garetto, C. R. Apesteguia, and B. Moraweck, The Journal of Physical Chemistry **100**, 9068 (1996).

[16] F. C. Galisteo, R. Mariscal, M. L. Granados, J. Fierro, R. Daley, and J. Anderson, Applied Catalysis B: Environmental **59**, 227 (2005).

[17] Y. Nagai, K. Dohmae, Y. Ikeda, N. Takagi, T. Tanabe, N. Hara, G. Guilera, S. Pascarelli, M. a. Newton, O. Kuno, et al., Angewandte Chemie (International ed. in English) **47**, 9303 (2008).

[18] G. Ertl, Angewandte Chemie (International ed. in English) **48**, 6600 (2009).

[19] A. Sault and V. Tikare, Journal of Catalysis **211**, 19 (2002).

[20] E. Kovalyov and V. Elokhin, Chemical Engineering Journal **154**, 88 (2009).

[21] G. Prévot, Physical Review B **84**, 1 (2011).

[22] P. Wynblatt and N. Gjostein, Acta Metallurgica **24**, 1165 (1976).

[23] I. M. Lifshitz and V. V. Slyozov, Journal of Physics and Chemistry of Solids **19**, 35 (1961).

[24] C. Wagner, Zeitschrift für Elektrochemie, Berichte der Bunsengesellschaft für physikalische Chemie **65**, 581 (1961).

[25] B. K. Chakraverty, Journal of Physics and Chemistry of Solids **28**, 2401 (1967).

[26] C. T. Campbell, S. C. Parker, and D. E. Starr, Science (New York, N.Y.) **298**, 811 (2002).

[27] S. Parker and C. Campbell, Physical Review B **75**, 1 (2007).

[28] E. E. Gruber, Journal of Applied Physics **38**, 243 (1967).

[29] L. E. Willertz and P. G. Shewmon, Metallurgical Transactions **1**, 2217 (1970).

[30] B. Pulvermacher and E. Ruckenstein, Journal of Catalysis **29**, 224 (1973).

[31] E. Ruckenstein and B. Pulvermacher, AIChE Journal **19**, 356 (1973).

[32] C. G. Granqvist and R. A. Buhrman, Journal of Applied Physics **47**, 2200 (1976).

[33] T. W. Hansen, Ph.D. thesis, Technical University of Denmark (2006).

[34] M. Zinke-Allmang, L. C. Feldman, S. Nakahara, and B. A. Davidson, Physical Review B **39**, 7848 (1989).

[35] G. Rosenfeld, K. Morgenstern, M. Esser, and G. Comsa, Applied Physics A: Materials Science & Processing **69**, 489 (1999).

[36] S. B. Simonsen, I. Chorkendorff, S. Dahl, M. Skoglundh, J. Sehested, and S. Helveg, Journal of the American Chemical Society **132**, 7968 (2010).

[37] A. K. Datye, Q. Xu, K. C. Kharas, and J. M. McCarty, Catalysis Today **111**, 59 (2006).

[38] S. E. Wanke, Journal of Catalysis **46**, 234 (1977).

[39] V. P. Zhdanov, Surface Review and Letters **15**, 217 (2008).

[40] L. R. Houk, S. R. Challa, B. Grayson, P. Fanson, and A. K. Datye, Langmuir **25**, 11225 (2009).

[41] P. Wynblatt and N. Gjostein, Progress in Solid State Chemistry **9**, 21 (1975).

[42] C. H. Bartholomew, Applied Catalysis A: General **107**, 1 (1993).

[43] G. A. Fuentes and E. D. Gamas, in *Catalyst Deactivation, Proceedings of the 5th International Symposium*, edited by C. H. Bartholomew and J. B. Butt (Elsevier, 1991), vol. 68, pp. 637–644.

[44] C. C. Chusuei, X. Lai, K. Luo, and D. W. Goodman, Topics in Catalysis **14**, 71 (2001).

[45] F. F. Tao and M. Salmeron, Science (New York, N.Y.) **331**, 171 (2011).

[46] A. I. Frenkel, J. A. Rodriguez, and J. G. Chen, ACS Catalysis **2**, 2269 (2012).

[47] S. Zhang, L. Nguyen, Y. Zhu, S. Zhan, C.-K. F. Tsung, and F. F. Tao, Accounts of chemical research **46**, 1731 (2013).

[48] J. Y. Park, *Current Trends of Surface Science and Catalysis* (Springer New York, New York, NY, 2014).

[49] J. C. Yang, M. W. Small, R. V. Grieshaber, and R. G. Nuzzo, Chem. Soc. Rev. **41**, 8179 (2012).

[50] H. Friedrich, P. E. de Jongh, A. J. Verkleij, and K. P. de Jong, Chemical reviews **109**, 1613 (2009).

[51] G. Prieto, J. Zecevic, H. Friedrich, K. P. de Jong, and P. E. de Jongh, Nature materials **12**, 34 (2013).

[52] S. Mostafa, F. Behafarid, J. R. Croy, L. K. Ono, L. Li, J. C. Yang, A. I. Frenkel, and B. R. Cuenya, Journal of the American Chemical Society **132**, 15714 (2010).

[53] B. Roldán Cuenya, J. R. Croy, S. Mostafa, F. Behafarid, L. Li, Z. Zhang, J. C. Yang, Q. Wang, and A. I. Frenkel, Journal of the American Chemical Society **132**, 8747 (2010).

[54] A. Carlsson, A. Puig-Molina, and T. V. W. Janssens, The Journal of Physical Chemistry B **110**, 5286 (2006).

[55] Z. Y. Li, N. P. Young, M. Di Vece, S. Palomba, R. E. Palmer, A. L. Bleloch, B. C. Curley, R. L. Johnston, J. Jiang, and J. Yuan, Nature **451**, 46 (2008).

[56] P. L. Hansen, J. B. Wagner, S. Helveg, J. R. Rostrup-Nielsen, B. S. Clausen, and H. Topsøe, Science (New York, N.Y.) **295**, 2053 (2002).

[57] P. Nolte, A. Stierle, N. Y. Jin-Phillipp, N. Kasper, T. U. Schulli, and H. Dosch, Science **321**, 1654 (2008).

[58] H. Yoshida, Y. Kuwauchi, J. R. Jinschek, K. Sun, S. Tanaka, M. Kohyama, S. Shimada, M. Haruta, and S. Takeda, Science (New York, N.Y.) **335**, 317 (2012).

[59] G. S. Parkinson, Z. Novotny, G. Argentero, M. Schmid, J. Pavelec, R. Kosak, P. Blaha, and U. Diebold, Nature materials **12**, 724 (2013).

[60] A. T. DeLaRiva, T. W. Hansen, S. R. Challa, and A. K. Datye, Journal of Catalysis **308**, 291 (2013).

[61] M. A. Asoro, D. Kovar, Y. Shao-Horn, L. F. Allard, and P. J. Ferreira, Nanotechnology **21**, 025701 (2010).

[62] R. T. K. Baker, Catalysis Reviews **19**, 161 (1979).

[63] S. R. Challa, A. T. Delariva, T. W. Hansen, S. Helveg, J. Sehested, P. L. Hansen, F. Garzon, and A. K. Datye, Journal of the American Chemical Society **133**, 20672 (2011).

[64] S. L. Y. Chang, A. S. Barnard, C. Dwyer, T. W. Hansen, J. B. Wagner, R. E. Dunin-Borkowski, M. Weyland, H. Konishi, and H. Xu, The Journal of Physical Chemistry Letters **3**, 1106 (2012).

[65] S. B. Simonsen, I. Chorkendorff, S. Dahl, M. Skoglundh, J. Sehested, and S. Helveg, Journal of Catalysis **281**, 147 (2011).

[66] K. Yoshida, Z. Xudong, A. N. Bright, K. Saitoh, and N. Tanaka, Nanotechnology **24**, 065705 (2013).

[67] L. F. Allard, S. H. Overbury, W. C. Bigelow, M. B. Katz, D. P. Nackashi, and J. Damiano, Microscopy and Microanalysis **18**, 656 (2012).

[68] J. F. Creemer, S. Helveg, G. H. Hoveling, S. Ullmann, A. M. Molenbroek, P. M. Sarro, and H. W. Zandbergen, Ultramicroscopy **108**, 993 (2008).

[69] J. F. Creemer, S. Helveg, P. J. Kooyman, A. M. Molenbroek, H. W. Zandbergen, and P. M. Sarro, Journal of Microelectromechanical Systems **19**, 254 (2010).

[70] N. D. Jonge, W. C. Bigelow, G. M. Veith, and N. de Jonge, Nano letters **10**, 1028 (2010).

[71] T. Yaguchi, M. Suzuki, A. Watabe, Y. Nagakubo, K. Ueda, and T. Kamino, Journal of electron microscopy **60**, 217 (2011).

[72] Y. Chen, R. E. Palmer, and J. P. Wilcoxon, Langmuir **22**, 2851 (2006).

[73] R. Wang, H. Zhang, M. Farle, and C. Kisielowski, Nanoscale **1**, 276 (2009).

[74] D. Alloyeau, T. Oikawa, J. Nelayah, G. Wang, and C. Ricolleau, Applied Physics Letters **101**, 121920 (2012).

[75] J. M. Yuk, M. Jeong, S. Y. Kim, H. K. Seo, J. Kim, and J. Y. Lee, Chemical communications (Cambridge, England) **49**, 11479 (2013).

[76] F. Behafarid and B. Roldán Cuenya, Surface Science **606**, 908 (2012).

[77] M. Bowker, Physical Chemistry Chemical Physics **9**, 3514 (2007).

[78] F. Yang, M. S. Chen, and D. W. Goodman, The Journal of Physical Chemistry C **113**, 254 (2009).

[79] F. Yang and D. W. Goodman, in *Scanning Tunneling Microscopy in Surface Science* (Wiley-VCH Verlag GmbH & Co. KGaA, 2009), pp. 55–95.

[80] W. Wallace, B. Min, and D. Goodman, Journal of Molecular Catalysis A: Chemical **228**, 3 (2005).

[81] L. K. Ono, B. Yuan, H. Heinrich, and B. Roldán Cuenya, Journal of Physical Chemistry C **114**, 22119 (2010).

[82] C. Barth, A. S. Foster, C. R. Henry, and A. L. Shluger, Advanced materials (Deerfield Beach, Fla.) **23**, 477 (2011).

[83] L. Spenadel and M. Boudart, The Journal of Physical Chemistry **64**, 204 (1960).

[84] S. E. Wanke, in *Progress in Catalyst Deactivation SE - 14*, edited by J. Figueiredo (Springer Netherlands, 1982), vol. 54 of *NATO Advanced Study Institutes Series*, pp. 315–328.

[85] H. Borchert, E. V. Shevchenko, A. Robert, I. Mekis, A. Kornowski, G. Grübel, and H. Weller, Langmuir **21**, 1931 (2005).

[86] A. Jentys, Physical Chemistry Chemical Physics **1**, 4059 (1999).

[87] J. J. Rehr, J. J. Kas, F. D. Vila, M. P. Prange, and K. Jorissen, Physical Chemistry Chemical Physics **12**, 5503 (2010).

[88] K. Paredis, L. K. Ono, F. Behafarid, Z. Zhang, J. C. Yang, A. I. Frenkel, and B. Roldán Cuenya, Journal of the American Chemical Society **133**, 13455 (2011).

[89] K. Paredis, L. K. Ono, S. Mostafa, L. Li, Z. Zhang, J. C. Yang, L. Barrio, A. I. Frenkel, and B. Roldán Cuenya, Journal of the American Chemical Society **133**, 6728 (2011).

[90] J. Matos, L. K. Ono, F. Behafarid, J. R. Croy, S. Mostafa, A. T. DeLaRiva, A. K. Datye, A. I. Frenkel, and B. Roldán Cuenya, Physical Chemistry Chemical Physics **14**, 11457 (2012).

[91] T. Rieker, A. Hanprasopwattana, and A. K. Datye, Langmuir **15**, 638 (1999).

[92] B. Ingham, T. H. Lim, C. J. Dotzler, A. Henning, M. F. Toney, and R. D. Tilley, Chemistry of Materials **23**, 3312 (2011).

[93] A. E. Russell, Faraday Discussions **140**, 9 (2009).

[94] M. C. Smith, J. A. Gilbert, J. R. Mawdsley, S. Seifert, and D. J. Myers, Journal of the American Chemical Society **130**, 8112 (2008).

[95] C. Langhammer and E. M. Larsson, ACS Catalysis **2**, 2036 (2012).

[96] R. M. J. Fiedorow, B. S. Chahar, and S. E. Wanke, Journal of Catalysis **51**, 193 (1978).

[97] S. B. Simonsen, I. Chorkendorff, S. Dahl, M. Skoglundh, K. Meinander, T. N. Jensen, J. V. Lauritsen, and S. Helveg, The Journal of Physical Chemistry C **116**, 5646 (2012).

[98] L. Ono, D. Sudfeld, and B. Roldán Cuenya, Surface Science **600**, 5041 (2006).

[99] L. K. Ono and B. Roldán Cuenya, Catalysis Letters **113**, 86 (2007).

[100] J. Thessing, J. Qian, H. Chen, N. Pradhan, and X. Peng, Journal of the American Chemical Society **129**, 2736 (2007).

[101] C. T. Campbell, Accounts of chemical research **46**, 1712 (2013).

[102] C. T. Campbell and J. R. V. Sellers, Faraday Discussions **162**, 9 (2013).

[103] D. Kalakkad, A. K. Datye, and H. Robota, Applied Catalysis B: Environmental **1**, 191 (1992).

[104] L. Kundakovic and M. Flytzani-Stephanopoulos, Journal of Catalysis **179**, 203 (1998).

[105] H. Shinjoh, M. Hatanaka, Y. Nagai, T. Tanabe, N. Takahashi, T. Yoshida, and Y. Miyake, Topics in Catalysis **52**, 1967 (2009).

[106] J. A. Farmer and C. T. Campbell, Science (New York, N.Y.) **329**, 933 (2010).

[107] M. Chen and L. D. Schmidt, Journal of Catalysis **55**, 348 (1978).

[108] T. Lee and Y. G. Kim, Journal of Catalysis **90**, 279 (1984).

[109] S. B. Simonsen, Ph.D. thesis, Technical University of Denmark (2011).

[110] R. Lamber and W. Romanowski, Journal of Catalysis **105**, 213 (1987).

[111] M. Rubel, M. Pszonicka, M. Ebel, A. Jabłoński, and W. Palczewska, Journal of the Less Common Metals **125**, 7 (1986).

[112] S. Horch, H. T. Lorensen, S. Helveg, E. Laegsgaard, I. Stensgaard, K. W. Jacobsen, J. K. Norskov, and F. Besenbacher, Nature **398**, 99 (1999).

[113] W. Ling, N. Bartelt, K. Pohl, J. de la Figuera, R. Hwang, and K. McCarty, Physical Review Letters **93**, 166101 (2004).

[114] R. Baker, Journal of Catalysis **63**, 523 (1980).

[115] P. A. Crozier, R. Wang, and R. Sharma, Ultramicroscopy **108**, 1432 (2008).

[116] P. J. F. Harris, Nature **323**, 792 (1986).

[117] M. A. Newton, C. Belver-Coldeira, A. Martínez-Arias, and M. Fernández-García, Nature materials **6**, 528 (2007).

[118] R. Ouyang, J.-X. Liu, and W.-X. Li, Journal of the American Chemical Society **135**, 1760 (2013).

[119] N. Chaâbane, R. Lazzari, J. Jupille, G. Renaud, and E. Avellar Soares, The Journal of Physical Chemistry C **116**, 23362 (2012).

[120] G. Renaud, R. Lazzari, and F. Leroy, Surface Science Reports **64**, 255 (2009).

[121] S. Giorgio, M. Cabié, and C. R. Henry, Gold Bulletin **41**, 167 (2008).

[122] M. A. Brown, E. Carrasco, M. Sterrer, and H.-J. Freund, Journal of the American Chemical Society **132**, 4064 (2010).

[123] M. C. R. Jensen, K. Venkataramani, S. Helveg, B. S. Clausen, M. Reichling, F. Besenbacher, and J. V. Lauritsen, The Journal of Physical Chemistry C **112**, 16953 (2008).

[124] S. Porsgaard, L. R. Merte, L. K. Ono, F. Behafarid, J. Matos, S. Helveg, M. Salmeron, B. Roldán Cuenya, and F. Besenbacher, ACS Nano **6**, 10743 (2012).

[125] F. Behafarid and B. Roldán Cuenya, Topics in Catalysis **56**, 1542 (2013).

[126] J. Rickard, L. Genovese, A. Moata, and S. Nitsche, Journal of Catalysis **121**, 141 (1990).

[127] E. Ruckenstein, Journal of Catalysis **41**, 303 (1976).

[128] E. Ruckenstein and Y. Chu, Journal of Catalysis **59**, 109 (1979).

[129] J. Stulga, Journal of Catalysis **62**, 59 (1980).

[130] I. Sushumna and E. Ruckenstein, Journal of Catalysis **108**, 77 (1987).

[131] R. Fiedorow and S. E. Wanke, Journal of Catalysis **43**, 34 (1976).

[132] M. F. L. Johnson and C. D. Keith, The Journal of Physical Chemistry **67**, 200 (1963).

[133] T. Lee and Y. G. Kim, Korean Journal of Chemical Engineering **2**, 55 (1985).

[134] G. Straguzzi, H. R. Aduriz, and E. Gigola, Journal of Catalysis **66**, 171 (1980).

[135] S. W. Weller and A. A. Montagna, Journal of Catalysis **20**, 394 (1971).

[136] P. Loof, B. Stenbom, H. Norden, and B. Kasemo, Journal of Catalysis **144**, 60 (1993).

[137] O. Alexeev, D.-W. Kim, G. W. Graham, M. Shelef, and B. C. Gates, Journal of Catalysis **185**, 170 (1999).

[138] Y. Chu and E. Ruckenstein, Journal of Catalysis **55**, 281 (1978).

[139] A. G. Graham and S. E. Wanke, Journal of Catalysis **68**, 1 (1981).

[140] M. Faraday, Philosophical Transactions of the Royal Society of London **147**, 145 (1857).

[141] C. Dahmen and G. von Plessen, Australian Journal of Chemistry **60**, 447 (2007).

[142] J. N. Anker, W. P. Hall, O. Lyandres, N. C. Shah, J. Zhao, and R. P. Van Duyne, Nature materials **7**, 442 (2008).

[143] K. M. Mayer and J. H. Hafner, Chemical reviews **111**, 3828 (2011).

[144] C. Langhammer, E. M. Larsson, B. Kasemo, and I. Zorić, Nano Letters **10**, 3529 (2010).

[145] E. M. Larsson, C. Langhammer, I. Zorić, and B. Kasemo, Science (New York, N.Y.) **326**, 1091 (2009).

[146] E. M. Larsson, S. Syrenova, and C. Langhammer, Nanophotonics **1**, 249 (2012).

[147] E. M. Larsson, J. Millet, S. Gustafsson, M. Skoglundh, V. P. Zhdanov, and C. Langhammer, ACS Catalysis **2**, 238 (2012).

[148] D. B. Williams and C. B. Carter, *Transmission Electron Microscopy-A Textbook for Materials Science* (Springer, 2009), 2nd ed.

[149] C. M. Herzinger, B. Johs, W. A. McGahan, J. A. Woollam, and W. Paulson, Journal of Applied Physics **83**, 3323 (1998).

[150] H. Fredriksson, Y. Alaverdyan, A. Dmitriev, C. Langhammer, D. Sutherland, M. Zäch, and B. Kasemo, Advanced Materials **19**, 4297 (2007).

[151] A. W. Grant, Q.-h. Hu, and B. Kasemo, Nanotechnology **15**, 1175 (2004).

Paper I

In situ plasmonic sensing of platinum model catalyst sintering on different oxide supports in O_2 and NO_2 atmosphere

Pooya Tabib Zadeh Adibi, Francesco Mazzotta, Tomasz J. Antosiewicz, Magnus Skoglundh, Henrik Grönbeck, and Christoph Langhammer

Submitted to *ACS Catalysis*

In situ Plasmonic Sensing of Platinum Model Catalyst Sintering on Different Oxide Supports in O_2 and NO_2 Atmosphere

Pooya Tabib Zadeh Adibi[1,3], Francesco Mazzotta[1], Tomasz J. Antosiewicz[1,4], Magnus Skoglundh[2,3], Henrik Grönbeck[1,3], and Christoph Langhammer[1*]

[1]*Department of Applied Physics,* [2]*Applied Surface Chemistry and* [3]*Competence Centre for Catalysis, Chalmers University of Technology, SE-41296 Göteborg, Sweden*

[4]*Centre of New Technologies, University of Warsaw, 02-089 Warsaw, Poland*

E-mail: *clangham@chalmers.se

Abstract

Improved understanding of thermal deactivation processes of supported nanoparticles via sintering is needed in order to increase the lifetime of catalysts. To monitor sintering processes under industrially relevant application conditions, *in situ* experimental methods compatible with elevated temperatures, high pressures and harsh chemical environments are required. Here, we demonstrate the applicability of *in situ* indirect nanoplasmonic sensing (INPS) combined with *ex situ* TEM to investigate the sintering of Pt model catalysts on flat alumina and silica supports in O_2 and NO_2 atmospheres in real time and under operating conditions. A universal, support- and sintering-environment-independent scaling of the correlation between INPS centroid signal and mean Pt particle size during

sintering is identified. Moreover, by means of finite-difference time-domain (FDTD) electrodynamics simulations, we establish a generic scaling approach to account for different inherent sensitivities of INPS sensor platforms featuring dielectric support layers with different refractive index.

Introduction

Heterogeneous catalysts are often realized as nanometer sized metal particles dispersed on high surface area oxides, such as alumina or silica. However, due to the large surface to volume ratio of small metal particles, they are prone to sinter or coalesce into large particles under operating conditions. This is a major cause of catalyst deactivation and leads to additional costs associated with either metal overloading or regeneration procedures.[1] Nanoparticle sintering is a complex physical and chemical phenomenon, which is controlled by several parameters such as particle size distribution, temperature, atmosphere, metal and physicochemical properties of the support. Detailed understanding of the mechanisms and kinetics of sintering is therefore desirable to derive new strategies to limit the effect of these processes.

Despite extensive research during the past decades, the detailed mechanisms of sintering are far from fully understood.[2] The slow progress in this area is related to the fact that the phenomenon depends on various parameters including metal-support interactions, support morphology and gas environment[3]. Furthermore, there is the sheer complexity of the governing processes and a lack of suitable experimental methods, which allow *in situ* scrutiny of sintering processes in real time and under relevant operating conditions. The latter is critical as it has been proven difficult to derive proper sintering mechanisms

based on *ex situ* and *post mortem* analysis of particle size distributions (PSDs) alone.[2,4] An important step in this direction is the recent developments of *in situ* microscopy and spectroscopy in catalysis, as summarized in a recent review by Zhang et al.[5] Among such *in situ* techniques, environmental transmission electron microscopy (ETEM) has emerged as one of the most common and powerful methods to investigate sintering processes, even though in most cases pressure limitations still apply.[6–14] Additionally, regardless of the applied pressure, (E)TEM studies of sintering processes of nanoparticles have to be carried out with great care in order to avoid potential detrimental effects of the high-energy electron beam. Among spectroscopic methods, extended X-ray absorption fine structure (EXAFS) has been demonstrated as a promising tool to gain structural and chemical information of particles during sintering in harsh environment.[15–17] Nevertheless, EXAFS requires synchrotron light and often complex analysis.

In this work, we utilize *in situ* indirect nanoplasmonic sensing (INPS)[18] to monitor, in real time, the sintering kinetics of Pt nanoparticle model catalysts on two different supports relevant in catalysis, namely silica (SiO_2) and alumina (Al_2O_3). The sintering is studied at elevated temperatures in atmospheric pressures including O_2 and NO_2, which are environments that are known to promote particle growth.[7,8,19] The INPS measurements are complemented with *ex situ* TEM analysis to derive correlations between the plasmon signal and catalyst particle size. The present work represents a significant extension of experimental conditions used in our initial proof-of-principle study,[19] and demonstrate that INPS is an efficient research tool for studies of sintering processes *in operando*.

Experimental and simulation methods

Indirect Nanoplasmonic Sensing

The INPS technique is a versatile optical spectroscopy platform for materials science and catalysis applications.[18,20,21] It employs "sensor chips" that are comprised of gold nanoparticles fabricated on a glass substrate (see below) and covered by a thin layer of oxide material that mimics the support of a real catalyst. These sensor chips are (once the catalyst nanoparticles have been deposited on top) then mounted in a comparably simple experimental setup (Insplorion X1 flow reactor system, Insplorion AB, Göteborg, Sweden) in which optical transmission/extinction through the nanofabricated "plasmonic" sensor chips is measured in real time.[19] The extinction spectra are recorded with a fiber-coupled fixed grating spectrometer (Avantes AvaSpec-1024). The spectral position of the plasmon peak is evaluated by tracking the centroid (*i.e*. the center of mass of the top part of the peak[22]) in real time using the Insplorer® software (Insplorion AB). In this way, real time sintering kinetic data can be obtained under realistic application/sintering conditions. As low-power near-visible light is used for illumination, the INPS technique is completely non-invasive. The INPS technology is based on the localized surface plasmon resonance (LSPR) phenomenon characteristic for (noble) metal nanoparticles. LSPR gives rise to strong absorption and scattering of near-visible light as well as significant enhancement of the local electric fields around the particle.[23] In a far field extinction or transmission measurement, the LSPR manifests itself as a distinct peak at a specific wavelength, which strongly depends on the composition, size and shape of metal particle, together with the dielectric environment.[24]

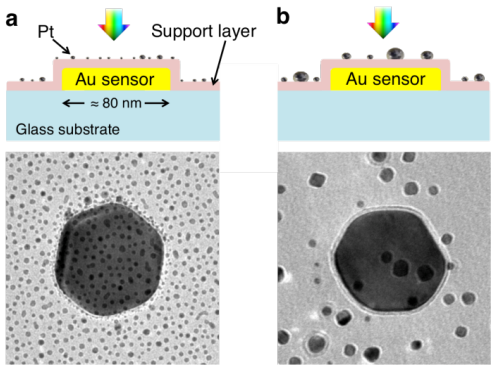

Figure 1: *Schematic picture and corresponding TEM images of indirect nanoplasmonic sensing (INPS) platforms before and after sintering. (a) Schematic cross-section of a gold sensor nanoparticle covered by a dielectric spacer layer comprising the INPS platform. Small Pt particles are grown on the dielectric spacer layer (i.e. the support). The corresponding TEM image shows the as-deposited Pt particles together with one INPS gold sensor particle that is covered with a 10 nm thick SiO_2 layer. (b) Same as (a) but after 12 h sintering treatment in O_2 at 600 °C during which the Pt particles rearrange on the sensor chip and, hence, change the effective refractive index around the sensor particles.*

The sensitivity towards local changes of the refractive index is the basis of nanoplasmonic sensing in general[25,26] and INPS in particular. In the present work, it is exploited to track the material rearrangements and consequent local nanoscale changes of the refractive index induced by the sintering process taking place on the INPS sensor surface. This is illustrated in Figure 1, which shows side-view schematic and corresponding TEM images of INPS arrangements with (panel a) as-deposited Pt particles, and of (panel b) Pt particles after sintering at elevated temperature. The images were obtained by fabricating the same structures as used on the "real" INPS chips onto TEM "windows" introduced in Ref. [27]. Direct TEM analysis of the INPS chips is not

possible as they are fabricated on 1 mm thick glass supports. In this context, it is also relevant to briefly discuss the possibility of alloy formation between the Au disk sensor and the Pt catalyst nanoparticles. In this study and also in our previous one[19] we find that the Pt volume on the sample is constant during the entire experiment, i.e. no mass loss occurs (Figure S1). This indicates that the thin dielectric layers indeed completely blocks mass transport between the Pt and the Au. Moreover, if we had migration of Pt (or any optically "lossy" metal) to the gold disk, we would expect this to contribute to a spectral redshift of the LSPR and we observe the opposite.

Sample fabrication

The INPS sensor chips consist of gold nano-disks with mean diameter of 80 nm and height of 20 nm. The discs are nanofabricated on fused silica substrates using hole-mask colloidal lithography[28]. As the plasmon resonance frequency of the gold sensors is shape-dependent, sensor-related plasmon peak shifts during the high-temperature experiments have to be prevented. For this purpose, the sensor chips were heat-treated at 800 $^{\circ}$C for 5 hours to stabilize the gold particles prior to the deposition of the oxide support layer. During the heat treatment, the gold nanodisks become faceted and attain stable hexagonal shapes (Figure S2). After the annealing, the oxide support material is deposited, and the sensor is further stabilized by a second heat treatment for 36 hours at 615 $^{\circ}$C in air. In this study, the considered support materials are 10 nm thick plasma-enhanced chemical vapor deposition (PECVD) grown silica and RF-sputtered alumina. For sputtering and PECVD, FHR MS 150 and STS tools were used, respectively. As the final step, Pt nanoparticles with average size of about 3.0 nm were grown on the two supports by means of thermal evaporation (deposition rate 0.05 nm/s) of an ultrathin granular Pt film with nominal

thickness of 0.5 nm. For this purpose, an AVAC HVC600 electron-beam evaporator operated at a base pressure of 3×10^{-6} mbar was used.

Finite difference time domain simulations

The optical measurement of the sintering process was simulated using the finite difference time domain (FDTD) method. Figure 2a illustrates the employed simulation scheme which comprises a 25 nm thick single gold disk with a bottom diameter of 60 nm and sidewall taper angle of 20 degrees. The substrate is a dielectric with $n = 1.45$. The disk and substrate are covered by a 10 nm thick spacer layer with a refractive index set to either $n = 1.48$ (silica) or 1.62 (alumina). Platinum nanoparticles are modeled as spheres with a uniform diameter equal to the mean size (3 nm) and particle density (2.5×10^{-4} nm^{-2}) derived from TEM images of samples before exposure to sintering conditions. The Pt spheres are placed uniformly on an area 200 nm by 200 nm. The structure, both with and without Pt nanoparticles, is illuminated by a total field/scattered field source 300 nm by 300 nm in size. The scattered energy flow and power dissipation are monitored to calculate scattering, absorption, and extinction cross-sections. To account for variability in Pt distribution, we performed five simulations with different Pt particle arrangement for each refractive index of the support layer for averaging. One simulation was performed for the case of a sample without Pt particles. The material properties are taken from the literature. Although the permittivity of small metal particles deviates from the corresponding bulk value,[29] we assume that this value is adequate enough to be used far away from the plasmon resonance. The current choice will underestimate losses[30].

Sintering conditions

For sintering in O_2, the samples were heated to 600 °C in Ar followed by a 10 min dwell in order to stabilize the temperature. After the temperature stabilization, the samples were exposed to 4% O_2 in Ar to initiate the sintering process. For the sintering experiments performed in NO_2, the temperature ramp in Ar was interrupted at 300 °C to expose the sample to 0.5% NO_2 for 15 minutes in order to stabilize the sensor chip in NO_2 atmosphere. We note that 300 °C is low enough so that no sintering occurs during the stabilization procedure. Following this pretreatment, a second temperature ramp to 600 °C in Ar was applied. After stabilization at 600 °C, 0.1%, NO_2 was introduced to induce Pt nanoparticle sintering. After the designated sintering time, the samples were cooled in Ar to avoid further sintering. Complete temperature and gas flow rate diagrams for the sintering experiments both in O_2 and NO_2 are presented in Figure S3. We note that the used O_2 and NO_2 concentrations are representative for the conditions in oxidation catalysts for automotives, which motivates our choice.

TEM imaging

The catalyst support materials, silica and alumina, were simultaneously deposited on silicon nitride TEM "windows"[27] and INPS chips for maximal comparability. The TEM window samples were then placed alongside the INPS samples in the flow reactor and exposed to identical gas and temperature conditions. Bright-field TEM analysis was then performed *post mortem* using an FEI Tecnai G2 instrument at 200 kV acceleration voltage. The projected areas of the imaged Pt particles were approximated by circles and outlined by ImageJ software to obtain mean particle diameter and particle density on the

surface. The contrast between the amorphous support and Pt particles arises mainly from the mass-thickness. The 40 nm thick silicon nitride membrane (on which the support and Pt particles are deposited) adds notable weight to the background mass-thickness, which makes it harder to determine the size of small particles with reasonable precision due to inadequate contrast. Thus, to avoid errors in the estimation of very small particles, only those larger than 1 nm^2 (in projection) are counted in the analysis. Typical obtained particle size distributions (PSDs) are shown in Figure S4.

Results and Discussion

Electrodynamics simulations

To understand the role of the refractive index of the support for the measured signal, we performed finite-difference time-domain (FDTD) electrodynamics simulations of the structures. Single gold disks on glass support, covered with a 10 nm thick dilelectric layer with refractive index corresponding to either silica or alumina and monodispersed 3 nm Pt spheres were simulated. The configuration mimics the beginning of the sintering experiments (Figure 2a). Figure 2b and c show the simulated extinction spectra corresponding to the LSPR response of a respective blank sensor (black dashed lines) and the response from sensors decorated with randomly distributed Pt spheres (green solid lines). For both support refractive index, the presence of the Pt spheres induces a spectral red-shift of the LSPR in the Au disk. The shift is larger for the support layer with the higher refractive index.

In Figures 2d and e, the top part of the LSPR peaks for a blank sensor and a sensor with Pt on top are magnified. The bottom x-axis is arranged so that the peak shift is set to zero

at the peak maximum for the blank sensor and shows again the larger red-shift of the LSPR peak upon Pt addition for the support layer with higher refractive index. Additionally, it is observed the different *local* arrangement of the Pt particles around the sensor in the corresponding 5 simulations slightly affects the LSPR peak position. However, this effect is small and does not affect the general conclusions. To address the effect of the refractive index of the support layer, the top (red) x-axis in Figures 2d and e is *scaled with the respective refractive index*. Comparing the peak positions for the sensors decorated with Pt on the scaled peak shift axes, reveals that they are identical after the scaling. This motivates the implementation of an identical scaling to the experimental data in order to account for the different sensitivities of INPS sensors featuring dielectric support materials with different refractive index.

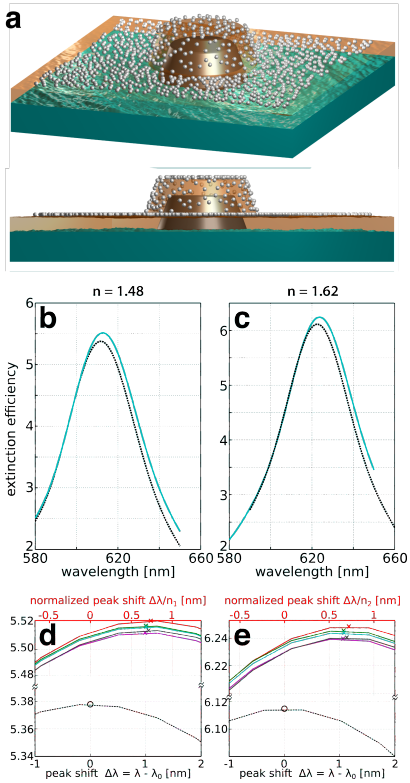

Figure 2. *FDTD simulations to clarify the role of the refractive index of the support layer. (a) Schematic depiction of the simulated arrangement. Randomly distributed Pt spheres with diameter D=3 nm decorate a gold sensor covered with a 10 nm thick support layer. (b) and (c) are simulated extinction of a single Au nanodisk on a glass support, covered by a 10 nm thick dielectric layer with refractive index n=1.48 (silica) or n=1.62 (alumina), respectively. The black dashed lines correspond to the LSPR response of a respective blank sensor. The green solid lines represent the response from sensors decorated with randomly distributed Pt spheres with diameter D=3 nm and particle density corresponding to the experimental ones for equivalent average particle size. Clearly, in both cases the presence of the Pt spheres induces a spectral red shift of the LSPR in the Au disk. The latter is larger for the support layer with the higher refractive index. (d) and (e) Zoom-in on the top part of the LSPR peaks for a blank sensor and a sensor covered with five different random arrangements of the Pt spheres at identical particle density. The bottom x-axis is arranged such that the peak shift is set to zero at the peak maximum for the blank sensor and shows again the larger red-shift of the LSPR peak upon Pt addition for the support layer with higher refractive index. The top (red) x-axis is scaled with the refractive index of the support and indicates that the support refractive index effect on the sensitivity of the INPS sensor efficiently can be cancelled out by scaling.*

Experimental results

The results from sintering of Pt particles on silica or alumina support and upon exposure to either 4% O_2 (alumina and silica) or 0.1% NO_2 (silica) in Ar at 600 °C for 6 hours are reported in Figure 3. The panels a-c show excerpts of the INPS-LSPR peaks for the considered systems at the beginning and end of the experiments. The discrete points correspond to the raw data from the spectrometer and the solid lines to the fitted polynomial functions used to determine the centroid readout signal. Clearly, a pronounced spectral blue-shift is observed for all three systems during sintering. The LSPR peak positions (that lies between 570 to 580 nm) differ slightly from the simulation values in Figure 2b and c. The main reason is the strong dependence of LSPR peak positions on the shape of plasmonic particles where in the FDTD simulation single gold sensor particle before heat treatment is modeled as disk, while in the experiments we exploited the stabilized (i.e. heat-treated) gold particles with hexagonal shape. Additionally, the amorphous nature of the used Au nanodisk arrays used in the experiment can shift the peak position both to the red and blue (compared to the simulated *single* disk) depending on the particle density in the array[31,32]. Importantly, however, the slight mismatch in peak position for either of these reasons will not affect the drawn conclusions.

Figure 3d shows the centroid shift measured with high temporal resolution. To account for the different sensitivities of the sensors due to the different refractive index of the support layer, the centroid signal is scaled with the support refractive index determined by ellipsometry (see Figure S5). The corresponding raw data without refractive index - scaling are shown in Figure S6. The INPS results for sintering of Pt particles on silica and

alumina in 4% O_2 are similar and the curve shapes resemble each other (blue and orange curve). In contrast, the sintering process of silica-supported Pt in 0.1% NO_2 appears to be much slower. Consequently, the refractive index-scaled centroid shift after 6 hours sintering in O_2 is almost double as compared to the corresponding shift for silica-supported Pt in 0.1% NO_2. This indicates a much more severe sintering in O_2 compared to NO_2 under the applied conditions. However, this is to be expected due to the lower NO_2 concentration. For reference, the signals from blank sensors without Pt exposed to the same conditions are also shown. Clearly, in contrast to the samples decorated with Pt nanoparticles, the signal is stable, *i.e.* no centroid shift is observed in neither O_2 nor NO_2 atmosphere.

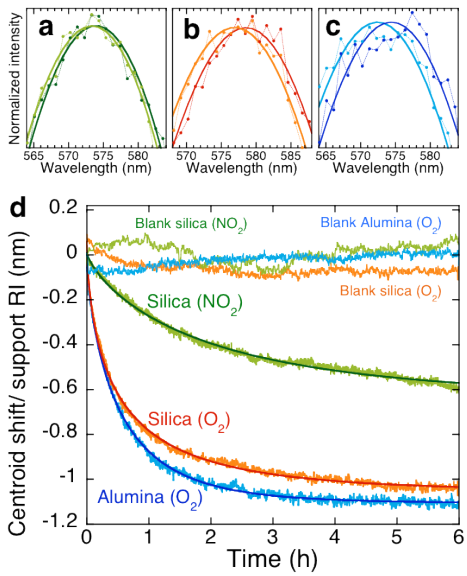

Figure 3: *Excerpts of experimentally measured LSPR peaks measured at the beginning of the sintering experiment and after 6 h of sintering for (a) silica-supported Pt in 0.1% NO_2, (b) silica-supported Pt in 4% O_2, and (c) alumina-supported Pt in 4% O_2. The discrete points correspond to the raw data from the spectrometer and the solid lines to the fitted polynomial functions used to determine the centroid readout signal. Clearly, a*

pronounced spectral blue-shift is seen for all three systems upon Pt particle sintering. (d) INPS sintering curves scaled with the refractive index of the support layer. The solid lines correspond to an exponential function fitted to the raw INPS curves. For all three systems a distinct negative shift of the centroid signal (corresponding to a spectral blue-shift of the plasmon resonance) indicates significant sintering. The result for sintering of Pt particles supported on silica and alumina in 4% O_2 is very similar and the curve shapes resemble each other (blue and orange curve). In contrast, the sintering process of silica-supported Pt in 0.1% NO_2 appears much slower and less severe._Corresponding INPS traces of blank sensors (i.e. no Pt) are also shown and exhibit a negligible centroid shift at the applied conditions.

As the next step of our analysis, a series of *ex situ* TEM images was taken for the different samples after specific time intervals along the 6 h total sintering experiments followed by INPS. As an example, Figure 4 shows TEM images of Pt nanoparticles before gas exposure and during aging at 600 °C on (a-d) alumina in 4% O_2, (e-h) silica in 4% O_2 and (i-l) silica in 0.1% NO_2. In the bright-field TEM images, the Pt particles appear as dark features. The initial particle size is fairly similar for all three systems, with the particles on alumina being the smallest ones. Clearly, with time, the particle density decreases while an increase in average diameter, <D>, and corresponding standard deviation are observed. This is in general agreement with the *in situ* INPS data shown in Figure 3d. Also in this data set, it is clear that the sintering kinetics in 0.1% NO_2 is much slower compared to 4% O_2. Analysis of the TEM images in terms of calculating particle volumes at different stages of the sintering furthermore shows that the total Pt volume is conserved during the experiment, i.e. that no Pt is lost to volatile PtO_x species (Figure S1). This is in good agreement with the study by Simonsen et al.[7], which showed Pt mass conservation during sintgering in oxidizing atmosphere at 650 °C. Notably their experiments were done on samples fabricated using the same evaporation system and the same amount of platinum as used in our study, which further strengthens the direct

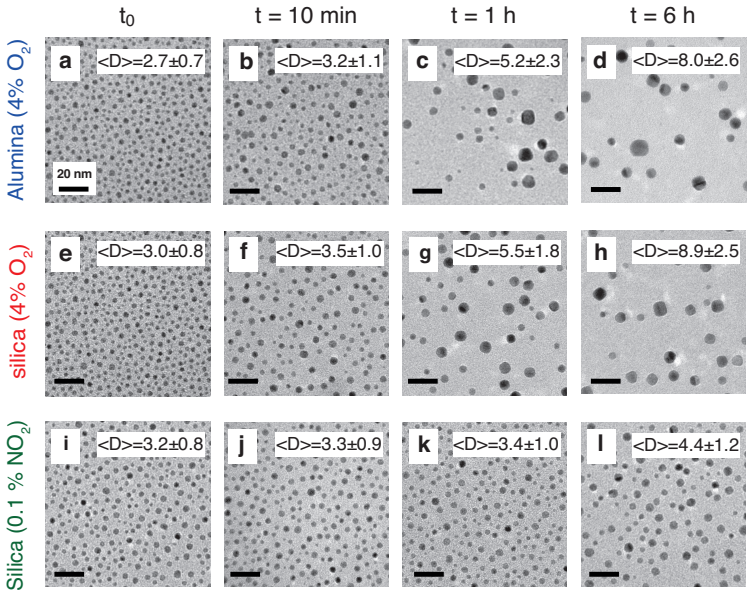

Figure 4: *Time-sequence of TEM images of Pt nanoparticles supported on (a-d) alumina and sintered in 4% O_2, (e-h) on silica and sintered in 4 % O_2, and (i,l) on silica and sintered in NO_2 at 600 °C. The scale bar in all images is 20 nm. A clear increase in average particle diameter, <D>, and corresponding decrease in particle density is seen. Note specifically the very similar sintering behavior of Pt particles on alumina and silica in O_2 in contrast to the less severe sintering of Pt particles on silica in NO_2 - in agreement with the scaled INPS centroid shift signal obtained in situ.*

relevance of their results for our data. Using this intermittent TEM data, it is now possible to "translate" the scaled INPS signals into the average particle diameter to obtain *in situ* sintering kinetics with high temporal resolution by constructing specific "translation" curves. To do this, the scaled centroid shifts corresponding to the sintering time after which the different TEM images were recorded, are in Figure 5 plotted versus the mean particle diameter. We then fit a function of type $\Delta\lambda = A + B\langle D\rangle^{-n}$ to the discrete points as shown by Larsson et al.[19] In this way, empirical calibration functions for the different systems are obtained. The calibration functions can be used to translate

the *in situ* INPS centroid signal to a high-resolution temporal evolution of the mean particle size during the sintering process. We obtain the following specific calibration functions for the three considered systems:

$\Delta\lambda = -1.07 + 22.62 \langle D \rangle^{-2.66}$ Silica (NO_2)

$\Delta\lambda = -1.21 + 10.34 \langle D \rangle^{-2.17}$ Alumina (O_2)

$\Delta\lambda = -1.15 + 13.96 \langle D \rangle^{-2.29}$ Silica (O_2)

Interestingly, it becomes clear from comparing the obtained functions, as well as from visual inspection of Figure 5a, that the correlations between the scaled INPS signal and the mean particle diameter are very similar, and thus, almost of "universal" nature. The only difference is basically the slightly different initial particle diameters in the three data sets. This observation indicates two important findings: (i) the experimental approach is very robust and can indeed be applied when using different catalyst support materials and investigating sintering processes in different gas environments; (ii) that it may eventually be possible, by collecting more data, to derive a truly universal calibration function linking the centroid shift signal with mean particle size, where the *initial* particle size before sintering is the only input required. However, this endeavor is beyond the scope of the present work as it would require significantly larger theoretical efforts to better understand the role of, *e.g.*, sintered particle shape and size distribution in the obtained INPS response.

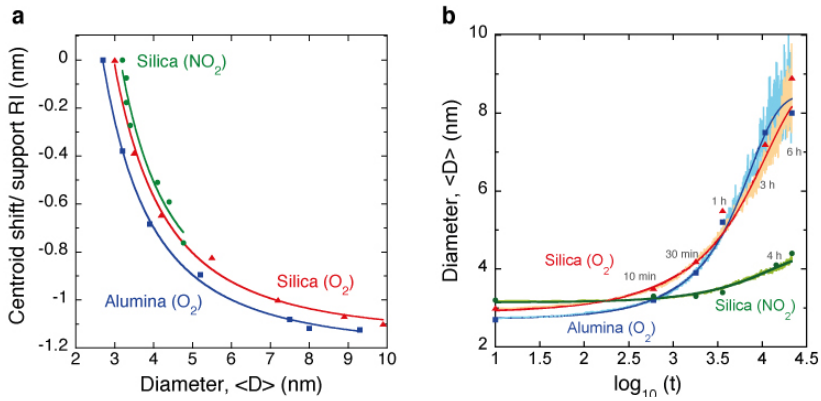

Figure 5: *(a) Correlation between refractive index -scaled INPS centroid signal and mean particle diameter <D> obtained from intermittent TEM data for sintered Pt particles on silica and alumina in 4% O_2 and 0.1 % NO_2 atmosphere. The solid lines are obtained by fitting a function of the form $\Delta\lambda = A + B<D>^{-n}$ to the experimental data points, as suggested by Larsson et al.*[19] *The latter yields an analytic expression that can be used to "translate" the INPS centroid signal to mean particle size, <D>, in order to derive the sintering kinetics with high temporal resolution. We note the almost "universal" nature of the obtained calibrations, i.e. their independence from both used support and applied gas environment. (b) High resolution real time experimental sintering kinetic data (solid lines) obtained by translating the centroid shift measured in situ during 6 h sintering experiments to mean particle size, <D>, using the derived translation functions from the analysis in panel (a). The dark full lines correspond to fitted exponential functions to the raw data and serve as a guide to the eye. The discrete points show the mean particle diameter derived from TEM.*

In the last analysis step we use our calibration functions to convert the real time INPS centroid shift signals to mean particle diameter by the procedure described above. In this way, we obtain unique *in situ* sintering kinetic curves with unmatched temporal resolution that follow the rough trend given by the intermittently obtained TEM images over 6 hours of sintering (Figure 5b). The INPS technique, however, reveals the sintering process at a much higher level of detail.

Conclusions

In summary, the presented INPS experimental platform shows high potential to significantly alleviate the lack of robust and versatile experimental techniques to scrutinize the sintering of catalyst nanoparticles *in operando*. As the main result we find gas environment- and support layer material-independent correlations between Pt particle size and the measured centroid shift response of the INPS sensor during sintering by scaling the latter with the refractive index of the used support material. These correlations allow the derivation of high-resolution sintering kinetics in real time, which paves the way to use the INPS method for detailed *in situ* investigations of the role of (i) the catalyst support material and (ii) different gas environments in sintering processes. These obtainable insights will be critical to derive strategies for the development of sintering-resistant catalysts in the future.

Acknowledgements

We acknowledge financial support from the Competence Centre for Catalysis, which is financially supported by Chalmers University of Technology, the Swedish Energy Agency, and the member companies: AB Volvo, ECAPS AB, Haldor Topsøe A/S, Scania CV AB, Volvo Car Corporation AB, and Wärtsilä Finland Oy, the Swedish Research Council Project 2010-4041, the Chalmers Areas of Advance for Nanoscience and Nanotechnology and Transport, the Swedish Foundation for Strategic Research Framework Program RMA11-0037, the Polish National Science Center via the project 2012/07/D/ST3/02152, the EMRP researcher grant no. IND15-REG1, and the Knut and Alice Wallenberg Stiftelse for their support of the μ-fab cleanroom infrastructure in Sweden.

References

(1) Bartholomew, C. H. *Appl. Catal. A Gen.* **2001**, *212*, 17–60.

(2) Hansen, T. W.; Delariva, A. T.; Challa, S. R.; Datye, A. K. *Acc. Chem. Res.* **2013**, *46*, 1720–1730.

(3) Behafarid, F.; Roldan Cuenya, B. *Topics in Catalysis*. August 14, 2013, pp. 1542–1559.

(4) Datye, A. K.; Xu, Q.; Kharas, K. C.; McCarty, J. M. *Catal. Today* **2006**, *111*, 59–67.

(5) Zhang, S.; Nguyen, L.; Zhu, Y.; Zhan, S.; Tsung, C.-K. F.; Tao, F. F. *Acc. Chem. Res.* **2013**, *46*, 1731–1739.

(6) Asoro, M. A.; Kovar, D.; Shao-Horn, Y.; Allard, L. F.; Ferreira, P. J. *Nanotechnology* **2010**, *21*, 025701.

(7) Simonsen, S. B.; Chorkendorff, I.; Dahl, S.; Skoglundh, M.; Sehested, J.; Helveg, S. *J. Am. Chem. Soc.* **2010**, *132*, 7968–7975.

(8) Simonsen, S. B.; Chorkendorff, I.; Dahl, S.; Skoglundh, M.; Sehested, J.; Helveg, S. *J. Catal.* **2011**, *281*, 147–155.

(9) Challa, S. R.; Delariva, A. T.; Hansen, T. W.; Helveg, S.; Sehested, J.; Hansen, P. L.; Garzon, F.; Datye, A. K. *J. Am. Chem. Soc.* **2011**, *133*, 20672–20675.

(10) Chang, S. L. Y.; Barnard, A. S.; Dwyer, C.; Hansen, T. W.; Wagner, J. B.; Dunin-Borkowski, R. E.; Weyland, M.; Konishi, H.; Xu, H. *J. Phys. Chem. Lett.* **2012**, *3*, 1106–1110.

(11) Benavidez, A. D.; Kovarik, L.; Genc, A.; Agrawal, N.; Larsson, E. M.; Hansen, T. W.; Karim, A. M.; Datye, A. K. *ACS Catal.* **2012**, 2349–2356.

(12) Yoshida, K.; Xudong, Z.; Bright, A. N.; Saitoh, K.; Tanaka, N. *Nanotechnology* **2013**, *24*, 065705.

(13) Creemer, J. F.; Helveg, S.; Hoveling, G. H.; Ullmann, S.; Molenbroek, a M.; Sarro, P. M.; Zandbergen, H. W. *Ultramicroscopy* **2008**, *108*, 993–998.

(14) Jonge, N. De; Bigelow, W. C.; Veith, G. M.; de Jonge, N. *Nano Lett.* **2010**, *10*, 1028–1031.

(15) Sanchez, S. I.; Menard, L. D.; Bram, A.; Kang, J. H.; Small, M. W.; Nuzzo, R. G.; Frenkel, A. I. *J. Am. Chem. Soc.* **2009**, *131*, 7040–7054.

(16) Roldan Cuenya, B.; Alcántara Ortigoza, M.; Ono, L.; Behafarid, F.; Mostafa, S.; Croy, J.; Paredis, K.; Shafai, G.; Rahman, T.; Li, L.; Zhang, Z.; Yang, J. *Phys. Rev. B* **2011**, *84*, 1–14.

(17) Matos, J.; Ono, L. K.; Behafarid, F.; Croy, J. R.; Mostafa, S.; DeLaRiva, a T.; Datye, a K.; Frenkel, a I.; Roldan Cuenya, B. *Phys. Chem. Chem. Phys.* **2012**, *14*, 11457–11467.

(18) Langhammer, C.; Larsson, E. M.; Kasemo, B.; Zorić, I. *Nano Lett.* **2010**, *10*, 3529–3538.

(19) Larsson, E. M.; Millet, J.; Gustafsson, S.; Skoglundh, M.; Zhdanov, V. P.; Langhammer, C. *ACS Catal.* **2012**, *2*, 238–245.

(20) Larsson, E. M.; Langhammer, C.; Zorić, I.; Kasemo, B. *Science* **2009**, *326*, 1091–1094.

(21) Langhammer, C.; Larsson, E. M. *ACS Catal.* **2012**, *2*, 2036–2045.

(22) Dahlin, A. B.; Tegenfeldt, J. O.; Hook, F. *Anal. Chem.* **2006**, *78*, 4416–4423.

(23) Bohren, C. F.; Huffman, D. R.; Clothiaux, E. E. *Absorption and Scattering of Light by Small Particles*; Wiley VCH Verlag GmbH, 2010.

(24) Mayer, K. M.; Hafner, J. H. *Chem. Rev.* **2011**, *111*, 3828–3857.

(25) Anker, J. N.; Hall, W. P.; Lyandres, O.; Shah, N. C.; Zhao, J.; Van Duyne, R. P. *Nat. Mater.* **2008**, *7*, 442–453.

(26) Larsson, E. M.; Syrenova, S.; Langhammer, C. *Nanophotonics* **2012**, *1*, 249–266.

(27) Grant, A. W.; Hu, Q.; Kasemo, B. *Nanotechnology* **2004**, *15*, 1175–1181.

(28) Fredriksson, H.; Alaverdyan, Y.; Dmitriev, a.; Langhammer, C.; Sutherland, D. S.; Zäch, M.; Kasemo, B. *Adv. Mater.* **2007**, *19*, 4297–4302.

(29) Carmina Monreal, R.; Antosiewicz, T. J.; Peter Apell, S. *New J. Phys.* **2013**, *15*, 083044.

(30) Lermé, J.; Baida, H.; Bonnet, C.; Broyer, M.; Cottancin, E.; Crut, A.; Maioli, P.; Del Fatti, N.; Vallée, F.; Pellarin, M. *J. Phys. Chem. Lett.* **2010**, *1*, 2922–2928.

(31) Antosiewicz, T. J.; Apell, S. P.; Zäch, M.; Zorić, I.; Langhammer, C. *Phys. Rev. Lett.* **2012**, *109*, 247401.

(32) Antosiewicz, T. J.; Apell, S. P. *Opt. Express* **2014**, *22*, 2031–2042.

Supporting information

1. *Pt mass conservation*

Figure S1 shows the Pt volume per area during different sintering time intervals. These values are obtained by assuming particles as spheres. However, this assumption is too simple as the particle shapes are subjected to change during sintering.[1] Therefore, relatively small fluctuation in the apparent volume is expected.

2. *Stability of INPS sensors*

The plasmon resonance frequency of the gold sensors depends on the shape of the particles. In order to stabilize the shape of gold sensor particles when exposed to high temperature, the sensor chip is heat treated at 800 °C for 5 hours. Figure S2 shows the gold particles before and after such heat treatment. The hexagonal shape of the particles after heat treatment (Figure S2 b) shows the equilibrium structure of the sensor particles.

3. *Sintering conditions*

Figure S3 represents the temperature and flow rate diagram for sintering experiments in NO_2 and O_2 experiments. As it could be seen in Figure S3 b, for NO_2 sintering measurements, the pretreatment in 0.5 % NO_2 at 300 °C for 15 minutes is preformed to stabilize the blank sensor.

4. *Refractive index measurement*

To determine the refractive index of support material (i.e. spacer layer of the INPS

sensors), spectroscopic ellipsometry (J.A. Woollam M-2000) is performed on 50 nm-thick sputtered alumina and PECVD silica layer that are deposited on single crystal silicon and followed by 36 hours heat treatment at 615 °C. A thicker layer compared to the support layer on the sensor (10 nm) is deposited for these measurements to eliminate the effect of interface layer between silicon substrate and the oxide.[2]

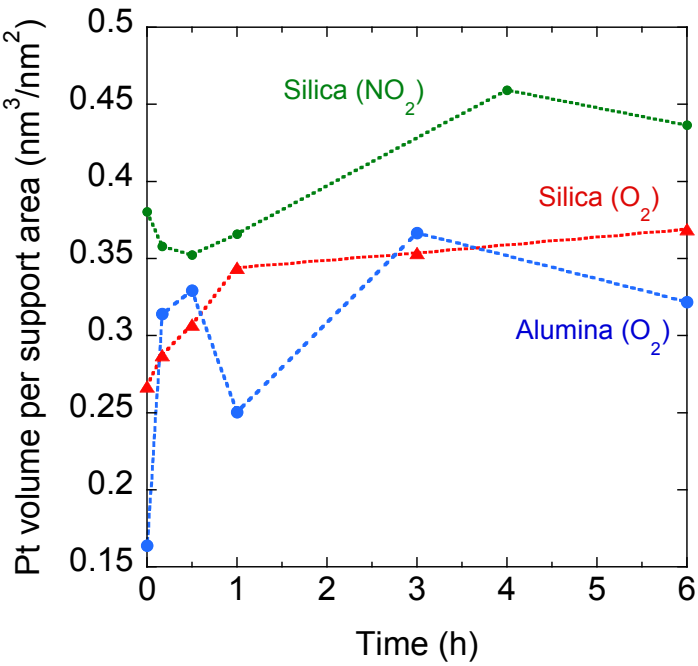

Figure S1. Platinum volume per support area as a function of sintering time for three studied cases.

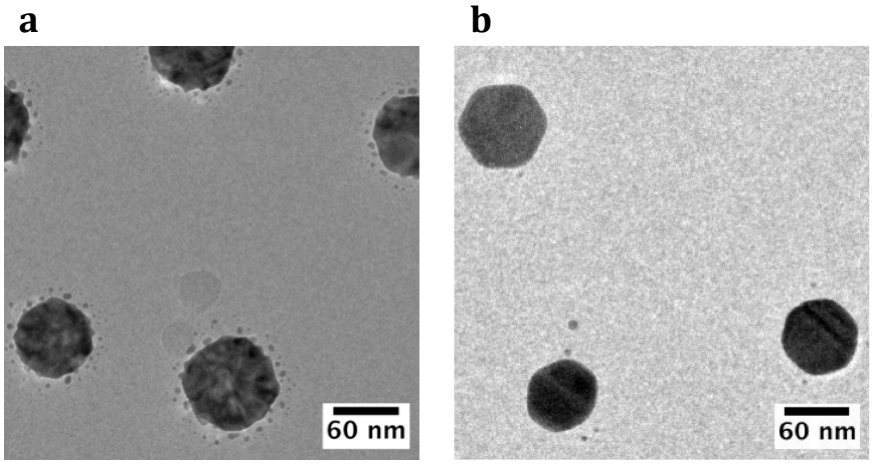

Figure S2: TEM images showing (a) gold sensor particles fabricated by hole-mask colloidal lithography, and (b) gold particles become faceted and thermally stable by 5 hours heat treatment at 800 °C.

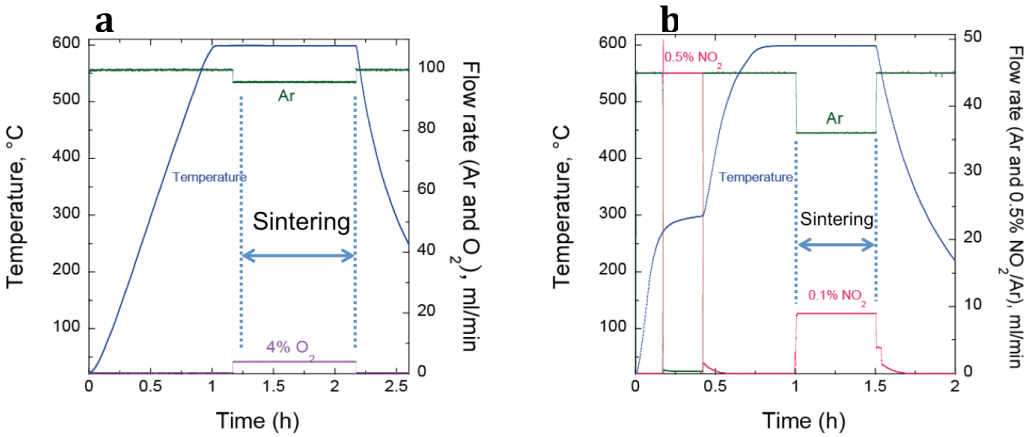

Figure S3: Temperature and flow rate diagram of sintering in (a) oxygen and (b) NO_2 environment. The total flow rate is 100 ml/min and 45 ml/min for sintering experiments in oxygen and NO_2, respectively, which is kept constant during the experiments.

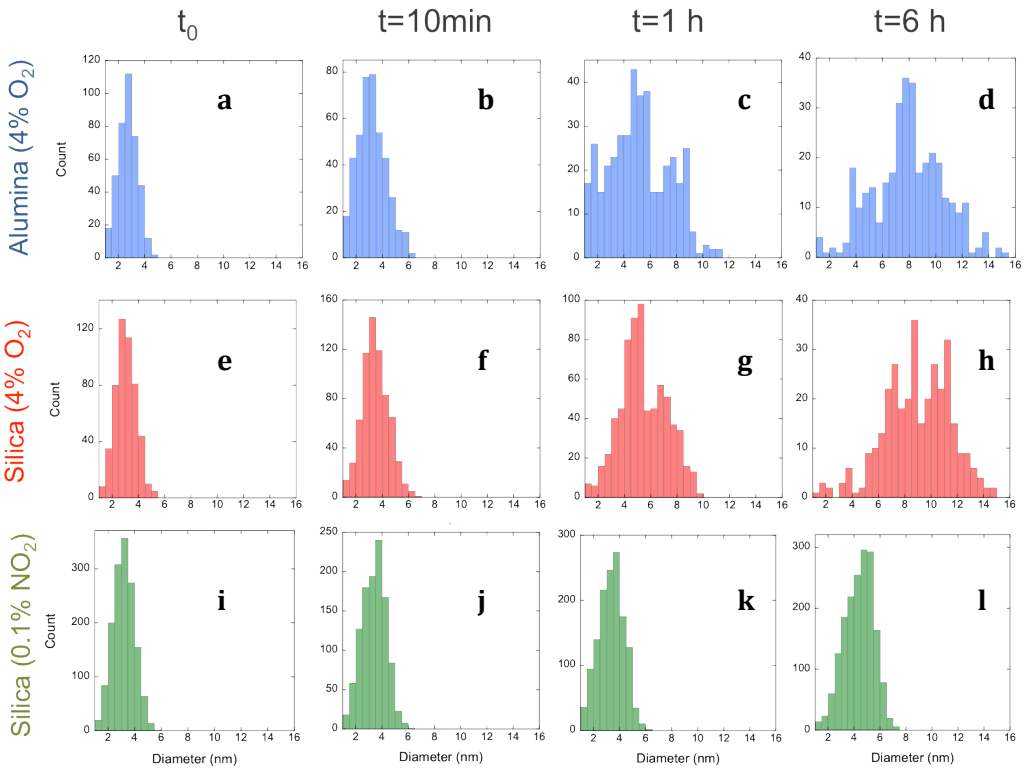

Figure S4: Particle size distributions of Pt nanoparticles supported on (a-d) alumina in 4% O_2, (e-h) silica in 4 % O_2 and (i,l) silica in NO_2 at 600 °C that corresponds to the TEM images in Figure 4.

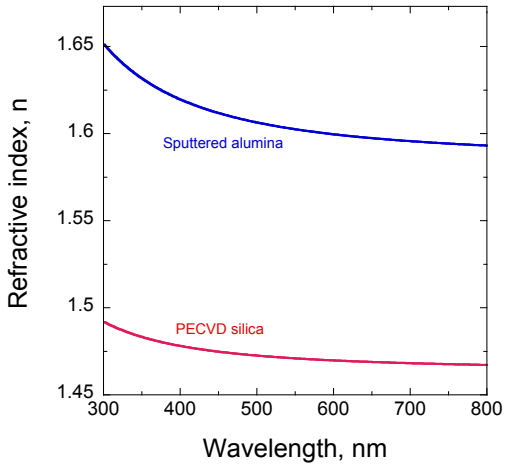

Figure S5: Spectroscopic ellipsometry of sputtered alumina and PECVD silica determines their refractive index. At the plasmon resonance wavelength (about 550 nm) of the sensors the refractive index of sputtered alumina and PECVD silica is found to be 1.62 and 1.48, respectively.

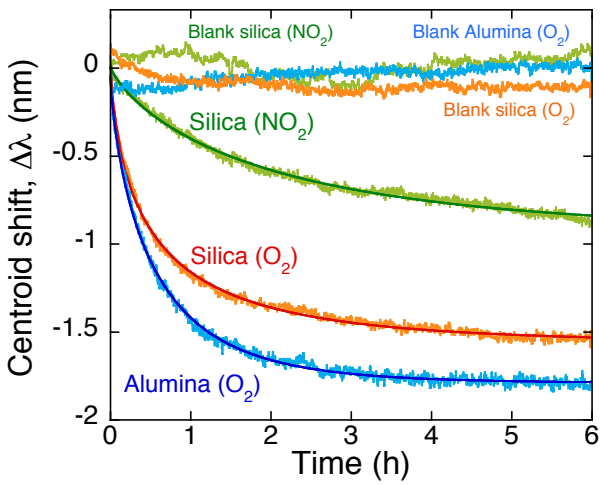

Figure S6: INPS centroid signal induced by the sintering of Pt nanoparticles on the sensor surface. The experiments were carried out at 600 °C in 4% O_2 in Ar for Pt supported on silica and alumina, and in 0.1% NO_2 in Ar on silica support. For all three systems a distinct negative shift of the centroid signal (corresponding to a spectral blue shift of the plasmon resonance) indicates significant sintering. Corresponding INPS

traces of blank sensors (i.e. no Pt) are also shown and exhibit a negligible centroid shift at the applied conditions. The solid lines correspond to an exponential function fitted to the raw INPS curves.

Reference:

(1) Simonsen, S. B.; Chorkendorff, I.; Dahl, S.; Skoglundh, M.; Meinander, K.; Jensen, T. N.; Lauritsen, J. V.; Helveg, S. *J. Phys. Chem. C* **2012**, *116*, 5646–5653.

(2) Herzinger, C. M.; Johs, B.; McGahan, W. a.; Woollam, J. a.; Paulson, W. *J. Appl. Phys.* **1998**, *83*, 3323.

Paper II

Transitional bimodal particle size distributions during Pt sintering on alumina and silica

Pooya Tabib Zadeh Adibi, Vladimir P. Zhdanov, Christoph Langhammer, and Henrik Grönbeck

In manuscript

Transitional bimodal particle size distributions during Pt sintering on alumina and silica

Pooya Tabib Zadeh Adibi[1,2], Vladimir P. Zhdanov[1,2,3], Christoph Langhammer[2], and Henrik Grönbeck[1,2,*]

[1] *Competence Centre for Catalysis,* [2] *Department of Applied Physics, Chalmers University of Technology, SE-41296 Göteborg, Sweden,* [3] *Russian Academy of Science, Boreskov Institute of Catalysis, Novosibirsk 630090, Russia*

E-mail:

Abstract

Sintering of Pt nanoparticles dispersed on alumina and silica during oxidizing conditions has been investigated by transmission electron microscopy. In particular, intermittent particle size distributions have been analyzed as a function of time and temperature. The analysis reveals transitional bi- and multimodal size distributions as the particles grow from 3 nm to about 10 nm. The study shows common features on the two supports and underlines the difficulties in deducing the dominant sintering mechanism from particle size distributions. Furthermore, the limitations of sintering models based on mean particle sizes are stressed.

*To whom correspondence should be addressed

Introduction

Heterogeneous catalysts are generally realized as metal particles dispersed on porous oxides such a alumina and silica. The surface area of the active metal phase is enhanced by preparing catalysts with nanometer sized particles. However, the large surface makes the systems inherently unstable and there is a strong thermodynamic driving force to reduce the surface area by coalescence into larger particles. In fact, this type of sintering is a major reason for thermal deactivation of catalysts which leads to a costly overloading of precious metals in applications.[1]

As thermal deactivation is a severe technological issue, it has received considerable attention over the years.[1] Fundamental studies have concentrated on the governing sintering processes and two main mechanisms have been put forward. One is based on the detachment of atoms or small units (monomers) from the metal particles. The monomers diffuse over the oxide surface (or via the gas phase) which eventually lead to the growth of some particles at the expense of others. This mechanism is generally referred to as Ostwald ripening (OR). The other mechanism is based on migration of entire particles that will coalesce into larger particles upon collisions (particle migration, PM). It is clear that also PM is governed by monomer diffusion but that the monomers in this case do not detach from the particles. Evidence for both processes has been observed[2] and the dominating mechanism depends on the considered system, or more precisely on the ratio between detachment energy (cohesive energy) and the adhesion of the monomers to the support.

Technical catalysts are generally prepared by wet impregnation where metal salts are decomposed at the oxide support. Even if such methods in principle, could lead to very high dispersions, the elevated temperatures that are required for the decomposition lead to atomic diffusion and an initial particle size distribution (PSD). In studies of sintering, the size distribution is often represented by some average particle radius $\langle R \rangle$. For technical catalysts, the radius is estimated indirectly by measurements of the particle dispersion via, for example, chemisorption experiments using CO or H_2.[3] The time evolution of the particle radius due to sintering is often

described by the phenomenological equation:

$$\langle R\rangle = (\langle R\rangle_0^n + n\,A\,t)^{1/n}.$$

Here, $\langle R\rangle_0$ is the initial average radius, whereas n and A are adjustable parameters. At sufficiently long times, the time dependence on the radius scales as $t^{1/n}$. In the case of OR, n is predicted[4] to be in the range between 3 and 4, whereas n is expected[5] to be between 5 and 7 for sintering due to PM. However, given that technical catalysts consist of metal particles with a certain size distribution, it could, in principle, be problematic to assign one average radius and follow the sintering kinetics by studying the time evolution of this parameter. It is not obvious that the average radius is a sensitive measure of the sintering kinetics. Furthermore, the governing mechanism could change as a function of particle size.

Studies of particle size distributions during sintering can enhance the understanding of governing mechanisms and several studies have appeared during recent years.[6–8] Such studies are mainly based on transmission electron microscopy (TEM) and have in some cases been performed on model catalysts with flat supports.[9–15]

Theoretical treatments of particle size distributions suggest that Ostwald ripening results in size distributions with a tail towards small sizes.[4] However, it should be mentioned that recent studies with a size dependent detachment energies, predict close to symmetric size distributions[16,17] or even distributions skewed to the right.[18] On the other hand, sintering arising from particle migration is predicted to yield log-normal distributions with a tail at larger sizes.[19] However, also in this case more recent studies indicate symmetric distributions.[5] Furthermore, it has experimentally been recognized that the sintering mechanism is difficult to deduce from studies of the particle size distributions.[20]

In careful analysis of particle size distributions, bimodal distributions have during recent years been observed in some cases.[8,14,21,22] Such distributions underline the complexity of sintering phenomena and the simplified view of the processes given by phenomenological equations such as (1). The basic reason for bimodal size distributions is surface heterogeneity.[23] This could, as in Ref.[23] be induced by a support having regions with different

monomer detachment and attachment energies or from a size dependent height-to-diameter ratio of the metal particles, Ref.[14]

In a recent study, we have investigated oxygen induced sintering of Pt particles supported on flat alumina and silica supports by indirect nanoplasmonic sensing (INPS).[24] Interestingly, it was concluded that the sintering kinetics on alumina and silica was very similar. Although INPS offers a convenient way for *in situ* monitoring of sintering kinetics,[22] it measures the average change of the metal particles without information on the particle size distributions. The particle size distributions are instead the focus of the present study. Here, detailed intermittent TEM analysis is performed during sintering of platinum on alumina and two types of silica. Sintering is studied both as a function time and temperature. On all samples, particles that initially have sharp size distributions centered at 3 nm sinter to mean particles sizes of about 10 nm via transitional bimodal distributions. Analysis of the average diameter with respect to equation (1) for Pt supported on alumina and sputtered silica shows an initial sintering via OR, whereas analysis of the full time range suggest PM. Our study stresses the difficulties in deducing the dominant sintering mechanism from both mean particle size and particle size distributions.

Experimental Methods

In order to facilitate TEM analysis, platinum particles were prepared on flat alumina and silica supports grown on electron-transparent silicon nitride TEM windows.[25] The alumina was obtained by Radio Frequency (RF) sputtering of aluminum in the presence of oxygen (FHR MS 150). Two types of silica were investigated, one using RF-sputtering of silicon and another using plasma-enhanced chemical vapor deposition (PECVD). In all cases the thickness of the oxides was about 10 nm as estimated by ellipsometry. The oxide layers were stabilized by a 36 h heat treatment at 615 °C in air. Finally, platinum particles were grown on the oxide supports by thermal evaporation with a deposition rate of 0.05 nm/s. This procedure results in an ultrathin granular Pt film with a nominal thickness of 0.5 nm. The evaporation was done using an AVAC HVC600 electron-beam evaporator operated

at a base pressure of 3×10^{-6} mbar.

The sintering experiments were performed in a gas flow reactor with a total flow rate of 100 ml/min. The samples were heated to a desired temperature (500, 550, or 600 °C) in Ar followed by a 10 min dwell time in order to stabilize the temperature. The temperature of the samples was monitored by a thermocouple. This treatment results in transformation of the as deposited platinum islands into the round nanoparticles with a homogeneous size distribution. It should be noted that the particles do not change after the initial stabilization when exposed to Ar only. This was explicitly tested by measurements of the particle size distributions after exposure to Ar for 12 hours at 610 °C.[22]

Sintering in oxygen was studied by exposure of the samples to 4% O_2 in Ar for a desired time interval, *i.e.* 10 min, 30 min, 1 h, 3 h, 6 h, 12 h and 24 h. After each sintering intervals, the samples were cooled in Ar to avoid further sintering. Note that different samples were used for each time interval.

TEM analysis was performed after the sintering experiments using an FEI Tecnai G2 T20 with LaB_6 cathode at 200 kV acceleration voltage. Depending on the contrast, the projected areas of the imaged Pt particles were outlined either manually or automatically by use of the ImageJ software.[26] The mean particle diameter was determined by a circular approximation of the projected areas. To avoid errors in the estimation of very small particles, only particles larger than 1 nm^2 were included in the analysis. The bin size in all the histograms is 0.7 nm.

Experimental results

Time-resolved study

In order to follow the evolution of the particle size distributions samples were exposed to oxygen (4 % O_2 in Ar) at 600 °C for different durations. Figure 1 shows TEM images together with size histograms for the three studied supports. To facilitate the analysis of particles that grow and to have an appropriate accuracy in the regime of both small and large particles, the TEM magnification was changed during the analysis. A nominal magnification of 145 k was used up to 30 min, 97 k for 1-6 hours and 71 k for 12 and 24 hours.

The initial configuration (t0) corresponds to the PSD just before exposure to oxygen. (This was not measured for sputtered silica.) The histograms are analyzed with respect to the arithmetic mean diameter and the standard deviation, which are included in the Figure. The initial distributions of Pt particles on both silica and alumina exhibit a narrow Gaussian shapes centered around 3 nm. The general trend upon sintering, is an increase in the mean diameter. On alumina and PECVD silica it is about 10 nm after 24 hours, whereas it is about 8 nm on sputtered silica. The widths of the distributions are broadened upon sintering, however, roughly constant after 3 hours.

Considering the evolution of platinum particles on alumina in detail (Figure 1, left column), the initial distribution has a mean diameter of 2.7 ± 0.7 nm. After 10 minutes aging, particles with diameters larger than 5 nm have appeared and the distribution is widened mainly towards larges sizes. This general trend continues for 30 min and 1 hour with the interesting addition that the number of small particles (less than 2 nm) increases. Furthermore, the distribution contains more than one maximum. After 3 hours, there is a clear shift of the main peak to larger sizes and the distribution is fairly symmetric. A less symmetric profile is observed again for particles sintered for 6 and 12 hours. At the last stage (24 h), a more symmetrical distribution is observed again.

For the case of Pt supported on PECVD silica, the initial Gaussian distribution transforms into a PSD skewed slightly towards the larger sizes. A shoulder on the right side of the main peak is developed after 1 hour. At later stages (3, 6, 12 and 24 hours) almost symmetrical PSDs are recorded. After the final sintering time (24 h), the PDS contains particles larger than twice the average size, i.e. particles larger than 20 nm. Pt supported on sputtered silica shows bimodality in the PDS after 3 and 6 hours. Interestingly, after 12 hours aging a noticeable peak in small particle region (ca. 2 nm) is imaged that it becomes even more pronounced after 24 hours. This feature results in a decrease of the mean particle diameter.

One common feature of our results is the appearance of transitional bi- or multimodal size distributions. This is in agreement with

previous studies of platinum sintering on alumina which have revealed the evolution of bimodal distribution during aging at elevated temperatures in oxygen.[12,14] The degree of sintering, however, appears to be critically dependent on sintering conditions, as all particle sizes in Ref.[14] after 3 hours of sintering in oxygen at 600 °C are below 6 nm. The most probable reason for the difference with respect to the present results is the difference in oxygen partial pressure which was 2 mbar in Ref.[14] The dependence of sintering on oxygen partial pressure is well established.[4,27,28] Concerning the shapes of the particle size distributions, we do not find any clear matches between the observed PSDs and the traditional characteristic distributions based on the models for OR (tail towards smaller particles) or PM (tail towards larger particles). Instead, the TEM analysis shows time-dependent PSDs and appearance of transitional multimodal distributions.

For sintering on alumina and sputtered silica we observe the appearance of small particles upon sintering. This observation indicates metal redispersion.[29] Such events could on one hand be possible in the case of large enough interparticle distances and defective surfaces where particles can trap before attaching to another particle.[30] On the other hand, formation of platinum oxide with limited interaction to the metallic particles could effectively result in fragmentation or spreading of the particles over the support.[11]

The time evolution of the mean diameter is shown in Figure 2. For clarity, a magnification of the time dependence during the first hour is given as an inset. Traditionally, this type of data has been fitted to equation (1) in order to obtain n, and thus the possible sintering mechanism. Following this procedure, we find in the case of alumina and sputtered silica that the result is dependent on the used time interval. Fitting the mean diameters in the first 3, 6, 12, and 24 hours yields sintering order of 2, 3, 4, and 5, respectively. Following the routine, this would imply that OR is the main mechanism during initial sintering whereas PM is valid at later stages. However, given the shape of the PSD this is a problematic and simplified analysis. IN the case of platinum on PECVD silica, the corresponding n values upon fitting lie between 3 and 4.

Temperature-resolved study

After studying the time evolution of the PSD at a given temperature, we studied the effect of sintering temperature. Figure 3 shows the initial PSDs together with the distributions after 12 hours aging at 500, 550, and 600 °C. In this set of measurements, platinum was deposited on all the supports at the same time, yielding very similar initial PSDs. Despite the similar size distribution, the density (number of particles per nm^3) and the surface coverage of Pt particles on alumina is significantly higher as compared to the silica surfaces (see SI). This implies differences in three-dimensional shapes and might be related to differences in Pt wetting properties on alumina and silica.

Sintering of Pt on alumina at 500 °C does not induce changes in the mean particle diameter. However, the size distribution broadens with the appearance of both larger and smaller particles. A significant change in the size distribution is observed at 550 °C with a bimodal PSD. One peak is centered around 4 nm, whereas the other is at 10 nm. Finally at 600 °C, the distribution turns into a single peak centered at 10 nm. The main trends for the PSDs on both PECVD and sputtered silica are similar to the ones on alumina. They evolve from single peak distributions centred at 3 nm over transitional bimodal distributions at 550 °C to single peak distributions (centered at 10 nm) after sintering at 600 °C. One difference between the alumina and silica supports is that small particles to larger extent is preserved on alumina. For example, at 500 °C, the mean diameter on alumina has not changed with respect to the initial state, whereas it has on the silica supports. Furthermore, the disappearance of the peak at 4 nm is slower on alumina as compared to silica. This indicates that alumina stabilizes platinum slightly better than the investigated silica supports. A large stabilization on alumina might be due to the higher degree of platinum wetting on alumina compared to silica supports (see SI).

In the present study we observe pronounced sintering at 550 °C on alumina. In the literature, sintering of platinum on alumina generally require temperatures higher than 600 °C. In fact, redispersion is in many cases observed for platinum supported on flat[9,11,13,30–32] and mesoporous[33–39] alumina exposed to oxygen

at temperatures below 600 °C. This stresses the importance of the chemical properties of the support for the sintering kinetics.

Conclusions

Sintering of Pt nanoparticles dispersed on alumina and silica during oxidizing conditions has been investigated by transmission electron microscopy. In particular, intermittent particle size distributions have been analyzed as a function of time and temperature. The analysis reveal transitional bi- and multimodal size distributions as the particles grow from 3 nm to about 10 nm. The study shows common features on the two supports and underline the difficulties in deducing the dominant sintering mechanism from particle size distributions. Furthermore, the limitations of sintering models based on mean particle sizes are stressed.

Acknowledgement

We acknowledge financial support from the Competence Centre for Catalysis, which is financially supported by Chalmers University of Technology, the Swedish Energy Agency, and the member companies: AB Volvo, Volvo Car Corporation AB, Scania CV AB, Haldor Topsøe A/S, ECAPS AB, and Wärtsilä Finland Oy.

References

(1) Bartholomew, C. H. *Applied Catalysis A: General* **2001**, *212*, 17–60.

(2) Hansen, T. W.; Delariva, A. T.; Challa, S. R.; Datye, A. K. *Accounts of chemical research* **2013**, *46*, 1720–30.

(3) Wanke, S. E. In *Progress in Catalyst Deactivation SE - 14*; Figueiredo, J., Ed.; NATO Advanced Study Institutes Series; Springer Netherlands, 1982; Vol. 54; pp 315–328.

(4) Wynblatt, P.; Gjostein, N. *Progress in Solid State Chemistry* **1975**, *9*, 21–58.

(5) Zhdanov, V. P. *Surface Review and Letters* **2008**, *15*, 217–220.

(6) Simonsen, S. B.; Chorkendorff, I.; Dahl, S.; Skoglundh, M.; Sehested, J.; Helveg, S. *Journal of the American Chemical Society* **2010**, *132*, 7968–75.

(7) Simonsen, S. B.; Chorkendorff, I.; Dahl, S.; Skoglundh, M.; Sehested, J.; Helveg, S. *Journal of Catalysis* **2011**, *281*, 147–155.

(8) Behafarid, F.; Roldan Cuenya, B. *Surface Science* **2012**, *606*, 908–918.

(9) Ruckenstein, E.; Malhotra, M. L. *Journal of Catalysis* **1976**, *41*, 303–311.

(10) Chu, Y.; Ruckenstein, E. *Journal of Catalysis* **1978**, *55*, 281–298.

(11) Ruckenstein, E.; Chu, Y. *Journal of Catalysis* **1979**, *59*, 109–122.

(12) Bellare, A.; Dadyburjor, D.; Kelley, M. *Journal of Catalysis* **1989**, *117*, 78–90.

(13) Rickard, J.; Genovese, L.; Moata, A.; Nitsche, S. *Journal of Catalysis* **1990**, *121*, 141–152.

(14) Simonsen, S. B.; Chorkendorff, I.; Dahl, S.; Skoglundh, M.; Meinander, K.; Jensen, T. N.; Lauritsen, J. V.; Helveg, S. *The Journal of Physical Chemistry C* **2012**, *116*, 5646–5653.

(15) DeLaRiva, A. T.; Hansen, T. W.; Challa, S. R.; Datye, A. K. *Journal of Catalysis* **2013**, *308*, 291–305.

(16) Parker, S.; Campbell, C. *Physical Review B* **2007**, *75*, 1–15.

(17) Prévot, G. *Physical Review B* **2011**, *84*, 1–9.

(18) Fuentes, G. A.; Salinas-Rodríguez, E. *Studies in Surface Science and Catalysis* **2001**, *139*, 503–510.

(19) Granqvist, C. G.; Buhrman, R. A. *Applied Physics Letters* **1975**, *27*.

(20) Datye, A. K.; Xu, Q.; Kharas, K. C.; McCarty, J. M. *Catalysis Today* **2006**, *111*, 59.

(21) Zhou, Y.; Zhou, J. *The Journal of Physical Chemistry Letters* **2010**, *1*, 609–615.

(22) Larsson, E. M.; Millet, J.; Gustafsson, S.; Skoglundh, M.; Zhdanov, V. P.; Langhammer, C. *ACS Catalysis* **2012**, *2*, 238–245.

(23) Zhdanov, V. P.; Larsson, E. M.; Langhammer, C. *Chemical Physics Letters* **2012**, *533*, 1–15.

(24) Tabib Zadeh Adibi, P.; Mazzotta, F.; Antosiewicz, T. J.; Skoglundh, M.; Grönbeck, H.; Langhammer, C. *ACS Catalysis, Submitted*

(25) Grant, A. W.; Hu, Q. H.; Kasemo, B. *Nanotechnology* **2004**, *15*, 1175–1181.

(26) Schneider, C. A.; Rasband, W. S.; Eliceiri, K. W. *Nature Methods* **2012**, *9*, 671–675.

(27) Bartholomew, C. H. *Applied Catalysis A: General* **1993**, *107*, 1–57.

(28) Ouyang, R.; Liu, J. X.; Li, W. X. *Journal of the American Chemical Society* **2013**, *135*, 1760–71.

(29) There might be a possibility that these particles were grown from very small particles that were not detectable in the TEM images.

(30) Stulga, J.; Wynblatt, P.; Tien, J. K. *Journal of Catalysis* **1980**, *62*, 59–69.

(31) Gollob, R.; Dadyburjor, D. *Journal of Catalysis* **1981**, *68*, 473–486.

(32) Sushumna, I.; Ruckenstein, E. *Journal of Catalysis* **1987**, *108*, 77–96.

(33) Johnson, M. F. L.; Keith, C. D. *The Journal of Physical Chemistry* **1963**, *67*, 200–201.

(34) Weller, S. W.; Montagna, A. A. *Journal of Catalysis* **1971**, *20*, 394–407.

(35) Fiedorow, R. M. J.; Wanke, S. E. *Journal of Catalysis* **1976**, *43*, 34–42.

(36) Fiedorow, R. M. J.; Chahar, B. S.; Wanke, S. E. *Journal of Catalysis* **1978**, *51*, 193–202.

(37) Straguzzi, G.; Aduriz, H. R.; Gigola, E. *Journal of Catalysis* **1980**, *66*, 171–183.

(38) Lee, T.; Kim, Y. G. *Journal of Catalysis* **1984**, *90*, 279–291.

(39) Lee, T.; Kim, Y. G. *Korean Journal of Chemical Engineering* **1985**, *2*, 55–61.

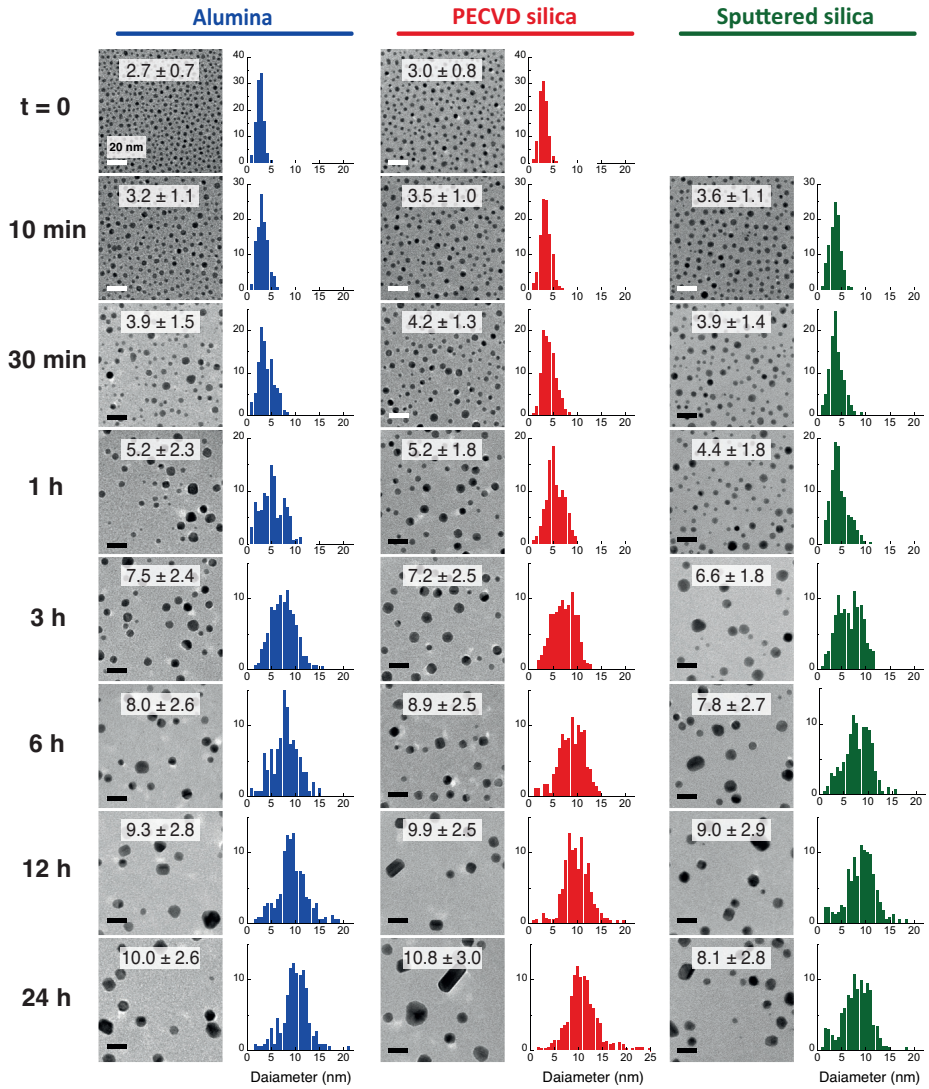

Figure 1: TEM images and corresponding particle size distribution of Pt particles supported on alumina, PECVD silica, and sputtered silica during sintering in 4 % O_2 at 600 °C after different time intervals. The scale bar on all images is 20 nm. The x-axis in the histograms represents the frequency of particles within each bin size.

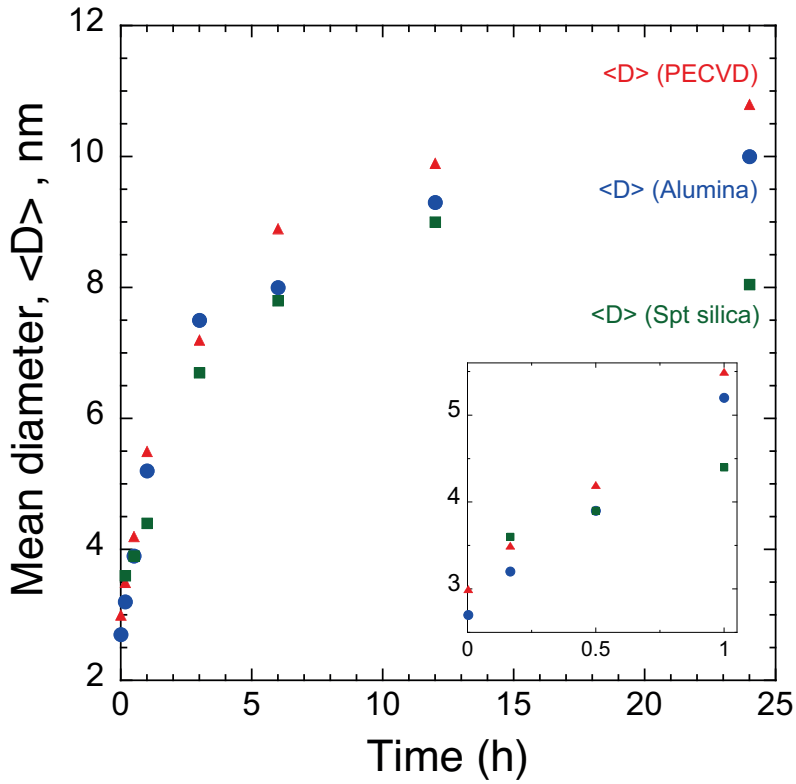

Figure 2: Mean diameters of Pt nanoparticles on three different support obtained form TEM analysis are plotted against the sintering time. Fitting the simple power law equation to different regions of the plot gives rise to different sintering order value, n.

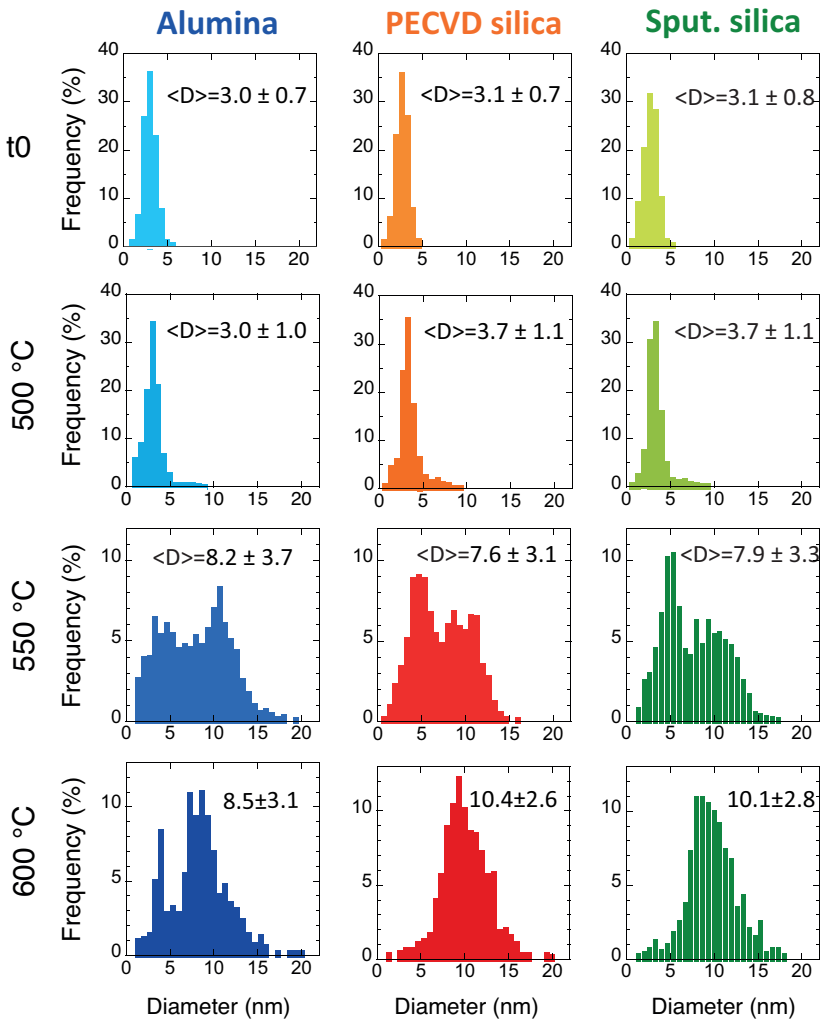

Figure 3: Particle size distribution of Pt particles supported on alumina, PECVD silica, and sputtered silica, (first row) before exposure to oxidizing environment, and (seond, third and last row) after 12 hours sintering in 4 % O_2 in Ar at 500, 550, and 600 °C.

Supporting Information

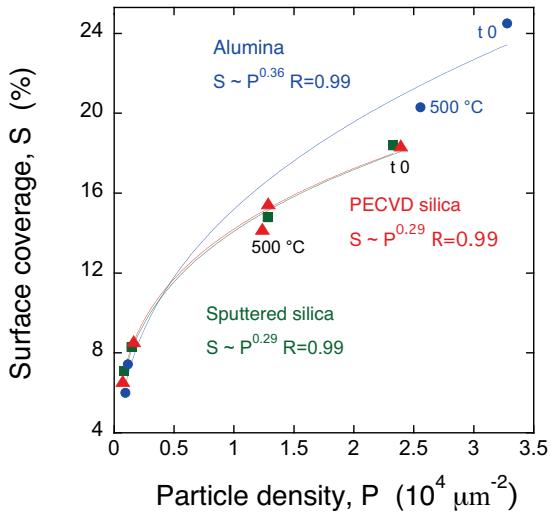

Figure 1: Surface coverage (S) vs. particle density (P) of Pt particles corresponding to the PSDs in Figure 3 (temperature-resolved study). Assuming spherical particles, the $S \sim P^{0.33}$ relation is expected.